

Gravitational Lensing Simulations I : Covariance Matrices and Halo Catalogues

Joachim Harnois-Déraps^{1,2*}, Sanaz Vafaei^{3†} and Ludovic Van Waerbeke^{3‡}

¹*Canadian Institute for Theoretical Astrophysics, University of Toronto, M5S 3H8, Canada*

²*Department of Physics, University of Toronto, M5S 1A7, Ontario, Canada*

³*Department of Physics and Astronomy, University of British Columbia, Vancouver, V6T 1Z1, B.C., Canada*

13 February 2012

ABSTRACT

Gravitational lensing surveys have now become large and precise enough that the interpretation of the lensing signal in current and future surveys has to take into account an increasing number of theoretical limitations and observational biases. Since much of the lensing signal is stronger in the non-linear scales, only numerical simulations can reproduce accurately enough the various effects one has to take into account. This work is the first of a series in which all gravitational lensing corrections known so far will be implemented in the same set of simulations using realistic mock catalogues. In this first paper, we present the TCS simulation suite and compare basic statistics such as the second and third order convergence and shear correlation functions to predictions for a large range of scales and redshifts. These simple tests set the range of validity of our simulations. We also compute the non-Gaussian covariance matrices of several statistical estimators, some of them are used in the Canada France Hawaii Telescope Lensing Survey (CFHTLenS). From the same realizations, we construct halo catalogues and present a series of halo properties that are required by most galaxy population algorithms.

Key words: cosmology: dark matter—weak lensing—large scale structure of Universe—methods: systematic

1 INTRODUCTION

The latest measurements of the cosmic microwave background (CMB) (Jarosik et al. 2011; Planck Collaboration et al. 2011) and of large scale galaxy surveys (York et al. 2000; Colless et al. 2003; Semboloni et al. 2006) are accurate enough to constrain most of the cosmological parameters at the few percent level. Observations seem to converge towards a standard model of cosmology, in which the Universe is mainly filled with a uniform dark energy component, and about a quarter of its energy distribution consists of dark matter (Percival et al. 2001; Eisenstein et al. 2005; Tegmark et al. 2006; Percival et al. 2007; Komatsu et al. 2011; Benjamin et al. 2007). The current knowledge about this dark sector is so limited that an international effort has been set forward in order combine the best techniques and optimize the global constraints on dark energy parameters (Albrecht et al. 2006). Next generation surveys including

LSST (LSST Science Collaborations et al. 2009), EUCLID (Beaulieu et al. 2010), SKA (Lazio 2008), Pan-STARRS¹, VST-KIDS², DES³ are designed to have very high quality data and large statistics, such that systematics and secondary effects need to be understood at the sub-percent level.

Weak lensing analyses, which are based on the measurement of the degree of deformation caused by foreground lenses on background light sources, are particularly praised to detect dark matter structures. The signal allows us to characterize the average mass profile of foreground lenses, which can consist of galaxies, groups or clusters of different type, redshift, morphology and color, typically centered on a dark matter halo. The signal from the 2-point cosmic shear depends on seven cosmological parameters, and is especially powerful at constraining a combination of the normalization of the matter power spectrum σ_8 and the matter density Ω_m . The degeneracy is further broken with measurements of the skewness and other higher-order statis-

* E-mail: jharno@cita.utoronto.ca

† E-mail: svafaei@phas.ubc.ca

‡ E-mail: waerbeke@phas.ubc.ca

¹ <http://pan-starrs.ifa.hawaii.edu/>

² <http://www.astro-wise.org/projects/KIDS/>

³ <https://www.darkenergysurvey.org/>

tics (Bernardeau et al. 1997). In the context of the global dark energy effort, high precision measurements of these two parameters are complimentary to other techniques (Baryonic Acoustic Oscillations, Type 1A Supernovae and cluster growth). It has recently been realized that weak lensing is also a standalone probe of the dark energy equation of state, through dependencies on the redshift-distance relation, the growth factor and the non-linear clustering (Huterer 2002; Albrecht et al. 2006; Hoekstra & Jain 2008). It is thus of the utmost importance to minimize the statistical, systematic and theoretical uncertainties associated with the signal.

The accuracy at which one can model this signal depends on the reliability of our understanding of the lenses and the sources, which in turn depends on the underlying matter density field, on the specific calculation of the light propagation, on the exact details of the galaxy population algorithm, and on our understanding of secondary effects. Early generations of calculations were performed within linear theory (see Bartelmann & Schneider 2001, for a review), which is known to underestimate the amount of structure in a large dynamical range. The projection of the density field on to a light cone causes the non-linear structures of the matter field to contribute to angles of a few tens of arc minutes for sources at redshift $z = 1$ (Jain et al. 2000). Better results were obtained from higher-order perturbation theory (Bernardeau et al. 2002), the halo model (Cooray & Sheth 2002) or with non-linear fitting formula (Smith et al. 2003). However these models generally fail at small angles, where the best measurements are obtained from N-body simulations (Blandford et al. 1991; Premadi et al. 1998; White & Hu 2000; Jain et al. 2000; Hilbert et al. 2009; Sato et al. 2009; Kiessling et al. 2011).

In addition, the description of the statistical uncertainty associated with weak lensing measurements needs to be as accurate as the signal itself, for the sake of robustness and constraining performance. The non-linear nature of the density field on small scales tends to correlate measurements that are otherwise independent. For instance, the Fourier modes of the density fields grow independently in the linear regime, but couple together in the trans-linear regime (Coles & Chiang 2000), which gives rise to non-Gaussian features in the power spectrum (Meiksin & White 1999; Rimes & Hamilton 2005; Neyrinck et al. 2006; Takahashi et al. 2009; Ngan et al. 2011; Harnois-Déraps & Pen 2011). These non-Gaussian signatures propagate in weak lensing measurements, as observed in simulations (Takada & Jain 2009; Doré et al. 2009; Sato et al. 2011) and in the data (Lee & Pen 2008), and have an effect on the power at which the lensing signal can constrain cosmology (Doré et al. 2009; Lu et al. 2010). The first goal of this paper is to provide robust non-Gaussian error bars on estimators commonly used in weak lensing analyses, including an accurate measurement of their non-linear covariance matrices. To match the resolution of modern surveys, our measurements must be accurate at the sub-arcminute level, thus deeply probing the non-linear regime.

One of the main limitation of the existing simulations is either that they are not resolving small enough scales, or they are limited in terms of number of realizations. For example, the Coyote Universe simulation suite (Lawrence et al. 2010) used cosmological volumes of $1300 h^{-1}$ Mpc per side, organized in three series for each cos-

mology. The ‘L-series’ consists of 16 realizations that cover to lower- k modes only, the ‘H-series’ covers the quasi-linear regime, and only one realization resolves the $k \ 1 h\text{Mpc}^{-1}$ scales. Also, the analyses carried by Kiessling et al. (2011) was based on the SUNGLASS pipeline (Kiessling et al. 2011) which relies on the GADGET2 tree-PM code. They used 100 simulations with 512^3 particles and a box size of $512 h^{-1}$ Mpc. Running a new series is necessary for no existing suite has both the statistics and the resolution required to extract estimates of the non-Gaussian covariance matrix on 2- and 3-points functions with sub arc-minute accuracy.

In this work, we are constructing the TCS simulation suite with CUBEP3M with eight times more particles than the above mentioned SUNGLASS series, in a volume more than forty times smaller, thus probing the non-linear regime much deeper. The resources that GADGET2 would require for our task is very large⁴, which explains why we opted for an alternative N-body code.

The second goal of this paper is to set the stage to start quantifying in details the main weak lensing secondary effects, which are often neglected, overlooked, and in any case have never been included all at once in the same simulated mock catalogues. With the forecasted accuracy of the next generation surveys, these need to be carefully examined, since they are likely to contribute to a large portion of the theoretical uncertainty. For instance, the impact of intrinsic alignment needs to be quantified in order to calibrate the lensing signal (Heymans et al. 2004). This effect is caused by the fact that galaxies that live in a same cluster are subject to a coherent tidal force, which tends to compress them along the direction to the centre of mass of the halo (Heavens & Peacock 1988; Schneider & Bridle 2010). Another secondary effect that needs to be examined is the so-called intrinsic alignment-lensing correlation (sometimes referred to shear-ellipticity correlation or contamination), a correlation that exists between the intrinsic alignment of the foreground galaxies and the shear signal of the same galaxies on background sources, provided the orientation of the foreground galaxy correlates with the tidal field it is subjected to (Hirata & Seljak 2004). Source clustering is another important secondary effect, which is caused by the fact that sources are not uniformly distributed : regions of the sky with more sources are likely to provide a stronger weak lensing signal (Bernardeau 1998). Also to be tested is the possible intrinsic alignment of galaxies with voids, an effect which was previously found to be consistent with zero (Heymans et al. 2006).

Many secondary effects have already been studied (Heymans et al. 2006; Semboloni et al. 2008), but the statistical accuracy and the resolution were limited. These previous works need to be extended. More importantly, these have been studied separately, and we do not yet understand how they blend together. The only way to accurately quantify their impact in the data is by measuring their combined contribution in accurate mock galaxy catalogues. There exists a variety of analytical methods to generate mock matter densities (Coles & Jones 1991; Scoccimarro & Sheth 2002)

⁴ For an estimator with N bins, the associated covariance matrix has N^2 entries, and will have converged if estimated with at least N^2 realizations.

which one can populate with galaxies, however these are incapable of reproducing accurately enough the non-linear dynamics, predominant at the galactic scale. N-body simulations, on the other hand, are perfectly suited for this exercise, as one can test separately the accuracy of the underlying density fields, the halofinder algorithm, the galaxy population scheme and the proposed weak lensing estimator (see Forero-Romero et al. (2007) for example). We thus plan to construct a large sample of mock galaxy catalogues with, in mind, to quantify the uncertainty on these secondary effects in a later stage.

This paper is addressing the first step in the construction, which is the determination of key properties of the underlying dark matter haloes, in the cosmological context under study. On the longer term, our catalogues can also be used to test new ideas that might contribute to the systematics of weak lensing signals. We do not attempt to measure all these effects here, but rather focus on the creation of the gravitational lenses and their associated halo catalogues, in order to set the scene for future work and know the limitations of our simulations. An interesting analysis, in the same spirit as that which we plan to perform, was carried in Semboloni et al. (2011), however we are improving both in statistics and resolution, plus we are extracting the covariance matrices on the estimators, and our objective is to include a number of secondary effects that were overlooked.

In this paper, however, we do not construct simulations that allows the study of baryonic feedback on the dark matter distribution. Recent work seems to suggest that effects such as AGN feedback and supernovae winds could impact noticeably the matter distribution in the Universe (Semboloni et al. 2011). Although this is something that could be significant for the interpretation of the lensing signal, especially at small angular scales, ignoring it does not diminish the value of studying the combined impact of the other lensing and systematics secondary effects mentioned before in the context of pure dark matter simulations. This is the path we have chosen to follow in our work. One could imagine that future generations of simulations could implement all the effects we are discussing here plus the effect of baryonic feedback.

This paper is organized as follows. In Section 2, we briefly review the theoretical background relevant for weak lensing studies, then we describe the design strategy of our simulations, as well as our numerical methods in Section 3. In Section 4, we test the performance of our simulated lines-of-sight. We present the weak lensing estimators and their non-Gaussian uncertainty in Sections 5 and 6. In Section 8, we describe the halo catalogues, and conclude in Section 9.

2 THEORY OF WEAK LENSING

In this section, we briefly review the theoretical background relevant for weak lensing numerical analyses. The propagation of a photon bundle emitted from a source located at β and observed at an angle θ in the sky is characterized by a Jacobian matrix $A(\theta)$:

$$A_{ij}(\theta) = \frac{d\beta_i}{d\theta_j} = (\delta_{ij} - \Psi_{ij}(\theta)) \quad (1)$$

where the matrix $\Psi_{ij}(\theta)$ encapsulates the distortion of the two dimensional image. It is determined by four components, namely a convergence κ , two shear components γ_1 and γ_2 that combine together into a complex shear $\gamma \equiv \gamma_1 + i\gamma_2$, plus an asymmetric factor ω . The latter comes from computing the distortion matrix to second order, but even then it has negligible contribution in realistic situations (see, for example, the Appendix of (Schneider et al. 1998)), hence we drop it. We thus write

$$\Psi = \begin{pmatrix} \kappa + \gamma_1 & \gamma_2 \\ \gamma_2 & \kappa - \gamma_1 \end{pmatrix} \quad (2)$$

All of these elements are locally determined by the Newtonian potential Φ via:

$$\kappa = \frac{\Phi_{,11} + \Phi_{,22}}{2}, \gamma_1 = \frac{\Phi_{,11} - \Phi_{,22}}{2}, \gamma_2 = \Phi_{,12} \quad (3)$$

where the ‘ i ’ refer to derivatives with respect to the coordinate i . For a source located at a comoving distance χ_s , the projected distortion is computed as:

$$\Psi_{ij} = \frac{2}{c^2} \int_0^{\chi_s} \Phi_{,ij} \frac{D(\chi)D(\chi_s - \chi)}{D(\chi_s)} d\chi \quad (4)$$

where c is the speed of light, and the comoving angular diameter distance $D(\chi)$ depends on the curvature:

$$D(\chi) = \begin{cases} K^{(-\frac{1}{2})} \sinh(K^{\frac{1}{2}}\chi) & \text{for } K > 0 \\ \chi & \text{for } K = 0 \\ -K^{(-\frac{1}{2})} \sin(-K^{\frac{1}{2}}\chi) & \text{for } K < 0 \end{cases} \quad (5)$$

with

$$K = \left(\frac{H_0}{c}\right)^2 (1 - \Omega_m - \Omega_\Lambda) \quad (6)$$

H_0 is Hubble’s parameter, Ω_m and Ω_Λ are respectively the ratio of the mass and dark energy densities to the critical density.

The convergence field is particularly interesting theoretically since it relates, through Poisson’s equation, to the density contrast δ :

$$\nabla^2 \Phi(\mathbf{x}) = \frac{3}{2} \Omega_m H_0^2 (1+z) \delta(\mathbf{x}) \quad (7)$$

with δ is defined as:

$$\delta(\mathbf{x}) = \frac{\rho(\mathbf{x}) - \bar{\rho}}{\bar{\rho}} \quad (8)$$

where $\bar{\rho}$ is the average matter density in the Universe and $\rho(\mathbf{x})$ is the local density. In the absence of curvature, the comoving angular diameter distance $D(\chi)$ takes the simplest form, and we can extract the projected convergence κ up to a distance χ_s as:

$$\kappa(\theta, \chi_s) \simeq \int_0^{\chi_s} W(\chi) \delta(\chi, \theta) d\chi \quad (9)$$

where $W(\chi)$ is defined as

$$W(\chi) = \frac{3}{2} \frac{\Omega_m H_0^2}{c^2} (1+z) g(\chi) \quad (10)$$

and

$$g(\chi) = \chi \int_\chi^\infty d\chi' n(\chi') \left(\frac{\chi' - \chi}{\chi'} \right) \quad (11)$$

The latter reduces to $\chi(1 - \frac{\chi}{\chi_s})$ when the source galaxies

are taken to reside in a single plane at χ_s . Otherwise, the source distribution $n(\chi)$ is taken to match observed surveys. In this paper, however, we use the single plane case both for illustrative purposes, and to disentangle cleanly the sources from the lenses.

From the convergence map, finally, one can extract the shear field by solving for the gravitational potential from [Eq. 3] (Kaiser & Squires 1993)⁵. In this process, one must be careful about the method used to perform this calculation, since the Universe is not periodic, while simulations usually are. The edge effects can therefore contaminate the calculations, hence it is necessary to somehow pad the boundaries.

3 NUMERICAL METHOD

As mentioned in the introductory section, gravity is a non-linear process, hence the predictions from the linear theory of large scale structures are only valid on the largest scales. In the context of the detection of weak lensing, photons trajectories are probing a broad dynamical range, and are indeed sensitive to galactic scale structures, where the matter fields are highly non-linear. Although higher-order perturbation theory can describe such systems, the accuracy of the calculations are limited by the complex dynamics. We thus rely on N-body simulations to generate reliable non-linear densities, then we propagate photons and extract the resulting image distortion matrix. In this section, we describe some of the considerations one must keep in mind when performing such calculations.

3.1 Tiling the lenses

Weak lensing simulations need to be optimized as a function of the specific measurements under study. In the current paper, we attempt to estimate the covariance matrix for a number of estimators, hence we need a large number of realizations, with a sub-arcminute accuracy. In an ideal world, one would simulate the complete past light cone that connects the observer to the light sources, for a given opening angle and pixel resolution. Unfortunately, for sources that extend to redshift of a few, this cannot be simulated all at once, since the far end of the cosmological volume is at an earlier time than the close end. It is, however, the only way one can model the largest radial modes of a survey. Luckily, these modes contribute very little to the weak lensing signal (Limber 1953). The coherence scales of the largest structures which contribute to the signal rarely extends over more than a few times the size of large clusters, so simulation box sizes of the order of a few hundreds of $h^{-1}\text{Mpc}$'s generally suffice to model the relevant structures. These simulated boxes can then be stacked as to create a pencil shaped volume, or a line-of-sight (LOS), inside of which photons are propagated.

One can use a different simulation for each redshift box, as done by (White & Hu 2000), but this method is

cpu consuming, since a single LOS involves running between 10 and 40 N-body simulations. For covariance matrix measurements, we need hundreds of these high precisions LOS, hence we opted for the common work around, which consists in treating different redshift density dumps of a single simulation as different sub-volumes of the same past light cone. Because the large scale structures evolve across redshift slices, there exists a systematic correlation between the lenses that can be minimized by randomly rotating the boxes and shifting the origin. This procedure allows us to reduce by at least an order of magnitude the number of simulations required for our measurements.

The next step consists in calculating the photon geodesics through the large scale structures, and to compute the cumulative deformation acquired along each trajectory. The most accurate calculations are performed by computing these geodesics in three dimensions, along their trajectory, starting from the observer's camera and progressing towards higher redshifts (Vale & White 2003). Such ray tracing methods provide one of the most reliable measurement of the cumulative shear, convergence and deflection angle measured at each pixel of the observer's camera, but need to be calculated at run time, or otherwise require to store the full density contrasts in memory. Cosmological codes that perform ray-tracing calculations at run time (Kiessling et al. 2011) typically run much slower, especially in high resolution of large volume simulations, and analyses that use the full three-dimensional densities (Vale & White 2003; Hilbert et al. 2009) have a large memory footprint, two limiting factors for the task at hand here.

However, it was shown (Vale & White 2003) that differences in lensing maps obtained from the mid-plane 'tiling' technique is less than 0.1 per cent, with nearly indistinguishable effects on the two- and three-point functions. This tiling approach consists in collapsing the cosmological sub-volumes into their mid-planes, creating two-dimensional slabs – or tiles – and calculating the geodesics on these thin lenses. Typically, all tiles have the same comoving dimension, and the past light cone is interpolated on to a set of pixels, whose sizes correspond to the angular resolution of the simulated telescope. In the weak lensing regime, these trajectories are close to straight lines, such that Born's approximation is very accurate (Schneider et al. 1998; Vale & White 2003). In this paper, we thus opt for a line-of-sight integration along the unperturbed photon paths. We nevertheless stored the full simulated lenses, allowing future analysis to test how much post-Born calculations (Schneider et al. 1998; Krause & Hirata 2010) affect the results.

Computations in this setting are fast, but not optimal: the interpolation becomes very strong at low redshift, thus increasing the impact of the simulation softening length. More over, a large portion of the simulated volume is left unused: the past light cone, shaped like a truncated pyramid, is extracted from a cuboid. We could in principle shuffle the projections axis and the origin once more to create additional LOS. However, this would inevitably produce a small amount of extra correlation between different realizations, that would propagate and contaminate the covariance matrix with extra non-Gaussian features. On the other hand, this would allow for hundred of additional, weakly correlated, LOS, which might be of use for future analyses that require even larger statistics.

⁵ For this operation, we are working under a flat sky approximation, which allows us to perform the Fourier transforms in the traditional plane wave basis, and to simplify the derivatives as a simple finite difference numerical calculation.

3.2 N-Body simulations

The N-body simulations are produced by CUBEP3M, an improved version of PMFAST (Merz et al. 2005) that is both MPI and OPENMP parallel, memory local and also allows for particle-particle (pp) interaction at the sub-grid level. 1024^3 particles are placed on a 2048^3 grid and their initial grid displacements and velocities are calculated from the Zel'dovich approximation (Zel'Dovich 1970; Shandarin & Zeldovich 1989) with a transfer function obtained from CAMB (Seljak & Zaldarriaga 1996). The following cosmological parameters are used both as simulation input and in our theoretical predictions : $\Omega_\Lambda = 0.721$, $\Omega_m = 0.279$, $\Omega_b = 0.046$, $n_s = 0.96$, $\sigma_8 = 0.817$ and $h = 0.701$.

As mentioned in the introduction, this work is meant to outperform the dynamical range of previous weak lensing simulations: we need sub-arc minute precision and a field of view of a few degrees per side. We designed our LOS such that each pixel has an opening angle of 0.21 arc minute on each side, with $n_{pix} = 1024^2$ pixels in total, for a total opening angle of 3.58° per side.

In order to reduce the wasted cosmological volume that falls outside the past light cone, we produced two sets of simulations, somehow following the strategy of (White & Hu 2000) – which used six box sizes to $z = 1$. It would be computationally too expensive to run that many distinct volumes, but we find that two box sizes offers a good trade off. High redshifts ($z > 1.0$) volumes are produced from simulations with a comoving side of $L = 231.1 h^{-1}\text{Mpc}$, while the low redshift ones are $L = 147.0 h^{-1}\text{Mpc}$ per side. These volumes are chosen such that the boundaries of the past light cone intersect with the edges of the smaller box exactly at $z = 1$ (in the given cosmology). The cone starts out at $z = 0$, then enters the larger volume, and meets its boundary at $z = 2.0$ (see Fig. 1). Some of the outer ray bundles eventually leave the simulated volume at larger redshifts larger than 2.0, in which case we enforce the periodicity of the simulations. This situation applies only to the last four lenses, hence the total amount of repeated structures is very small. This is even further suppressed by the lensing kernel, which favors redshifts closer to $z = 1 - 1.5$, and by the fact such high redshifts have much less galaxies to start with⁶.

With these choices of cosmological parameters and simulation volumes, the particle's mass in the large and small boxes are of 1.2759×10^9 and $3.2837 \times 10^8 M_\odot$ respectively, while the comoving sub-grid softening lengths r_{soft} are of 112.8 and $71.8 h^{-1}\text{kpc}$ ⁷.

The initial redshifts are selected such as to optimize both the run time and the accuracy of the N-body code. These are chosen to be $z_i = 40.0$ and 200.0 for the large and small box respectively. The reason for selecting different starting redshifts resides in the fact that the smaller box

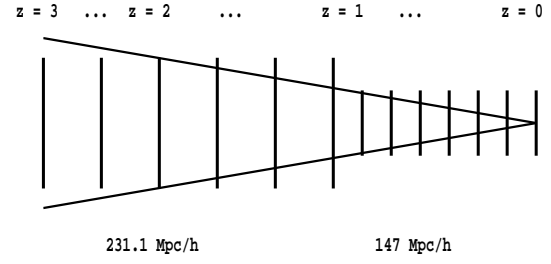


Figure 1. Geometry of the lines-of-sight. The global simulated volume consists of two adjacent rectangular prisms, collapsed as a series of thin lenses. As explained in the text, high redshift lenses have larger comoving volume, but the same number of grid cells, or pixels; this is meant to reduce the volume that falls outside of the past light cone. The observer sits at $z = 0$; the junction between the small (lower- z) and large (higher- z) simulation boxes occurs at $z = 1$; the past light cone escapes the simulated volume beyond $z = 2$, and we exploit the periodicity of the boundary condition to populate the edges of the most remote lenses and halo catalogues; we store lenses and haloes up to $z = 3$.

Table 1. Redshifts of the lenses. The projections for $z_l > 1.0$ are produced with $L = 231.1 h^{-1}\text{Mpc}$ simulations, while those for lower z_l are obtained from $L = 147.0 h^{-1}\text{Mpc}$, as described in the text.

3.004	2.691	2.411	2.159	1.933	1.728	1.542
1.371	1.215	1.071	0.961	0.881	0.804	0.730
0.659	0.591	0.526	0.463	0.402	0.344	0.287
0.232	0.178	0.126	0.075	0.025		

is probing smaller scales, hence it needs to start earlier, at a time where the Nyquist frequency of our grid is well in the linear regime. Each simulation is then evolved with `cubep3m` on 8 nodes of the Tightly Coupled System supercomputer at the SciNet HPC Consortium (Loken et al. 2010) – to which system we dedicate the name of the simulation suite. At each of the redshifts tabulated in Table 1, the dark matter particles are placed on to a 2048^3 grid using a ‘cloud-in-cell’ interpolation scheme (Hockney & Eastwood 1981). That grid is then collapsed in three different ways – along each of the 3 cartesian axes – producing triplets of slabs. These lens redshifts, z_l , are found by slicing into cubes our simulated volume, starting and ending at $z = 0.0$ and $z = 3.0$ respectively, and solving for the redshift at the centre of the comoving box.

With this configuration, we solve [Eq. 9] numerically for each pixel. We convert the χ integral into a discrete sum at the lens locations $\chi(z_l)$. The infinitesimal element $d\chi$ becomes dL/n_{grid} , where $n_{grid} = 2048$ and $L = 147.0$ or $231.1 h^{-1}\text{Mpc}$, depending on the redshift of the lens. Under the single source plane approximation, we can thus write the convergence field as

$$\kappa(\mathbf{x}) = \frac{3H_0^2\Omega_m}{2c^2} \sum_{z_l}^{z_s} \tilde{\delta}(\mathbf{x})(1+z_l)\chi(z_l)(1-\chi(z_l)/\chi(z_s))d\chi \quad (12)$$

where $\tilde{\delta}(\mathbf{x})$ is the two-dimensional density contrast.

To avoid edge effects when computing the shear fields,

⁶ We have used some of the otherwise wasted volume on occasions to extract lenses at low redshifts for some simulations that could not run until the end (reaching hard walltime limit, computer cluster downtime, etc.). In that process, we made sure that there were no overlap with the original lens.

⁷ r_{soft} is defined to be a tenth of a grid cell, and is enforced by a sharp cutoff in the force of gravity for particle pairs separated by smaller distances.

we perform the Fourier transforms on the full periodic slabs, i.e. *before* the interpolation on to the lenses.

4 TESTING THE SIMULATIONS

In this section, we quantify the resolution and accuracy of the simulated weak lensing simulations. We first measure the power spectrum of the simulated three dimensional density fields, i.e. before the collapse and pixel interpolation, and compare to the non-linear theoretical predictions of Smith et al. (2003)⁸. We then estimate the angular power spectrum of the simulated lines-of-sight, compare to non-linear predictions, and extract the effective resolution of the simulated fields.

4.1 Dark Matter Power Spectrum

The power spectrum of matter density $P(k)$ is a fast and informative test of the quality of the simulations. It probes the growth of structures at all scale available within the simulations, and comparison with a reliable theoretical models informs us of the accuracy and the resolution limit. For a given density contrast $\delta(\mathbf{x})$, the power spectrum can be calculated from its Fourier transform $\delta(\mathbf{k})$ as:

$$\langle \delta(\mathbf{k})\delta(\mathbf{k}') \rangle = (2\pi)^3 \delta_D(\mathbf{k} - \mathbf{k}') P(\mathbf{k}) \quad (13)$$

where the angle brackets refer a volume average, and the Dirac delta function selects identical Fourier modes. We present the power spectrum for our 185 simulations for two redshifts, $z = 0.961$ and $z = 0.025$, in Fig. 2. The error bars are the 1σ deviation in the sampling.

Resolution limits are mainly determined by the softening length in the gravitational force, and cause an abrupt drop in the observed power spectrum in small scales. In our simulations, we observe that the structures seem to be well model down to $k = 20.0 h\text{Mpc}^{-1}$, which corresponds to a comoving length of about $315 h^{-1} \text{ kpc}$. This drop of power can be modeled, following (Vale & White 2003), by a Gaussian filtering of the form $\exp[-k^2 \sigma_g^2]$ in the power spectrum, where $\sigma_g = 0.155L/N_{\text{grid}}$. This filter is in comoving coordinates, hence it is straight forward to calculate the angle subtended by $1\sigma_g$ at $z \sim 1.0$, the redshift that dominates the lensing kernel. From this rough estimate, we find that the softening angle is $\theta_{\text{soft}} = 0.148 \text{ arcsec}$. We note that this technique depends on the details of the N-body code, and that a more accurate estimate of the softening length can be found from a comparison of the angular power spectrum with non-linear theory, which we post-pone until section 4.2. Otherwise, we also observe that the higher redshift power is slightly on the low-side of predictions for $0.4 < k < 1.0 h\text{Mpc}^{-1}$, while the lower redshift power is slightly higher for $k > 1.0 h\text{Mpc}^{-1}$. These can be caused by a number of effects, from finite box size to residual uncertainty from numerical integration, and inevitably propagate in the calculations of past light cone. However, deviations from HALOFIT

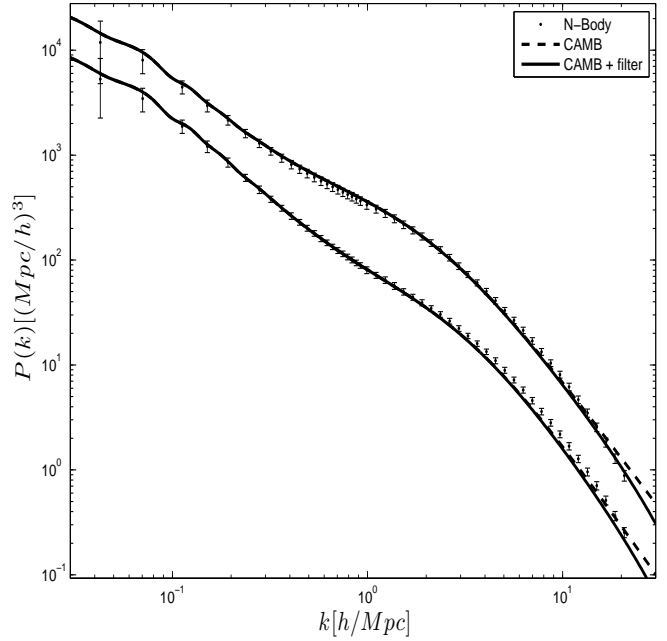


Figure 2. Power spectrum of 185 N-body simulations, at redshifts of 0.961 (bottom curve) and 0.025 (top curve). The solid and dashed lines are the non-linear predictions, with and without the Gaussian filter. The error bars shown here are the standard deviation over our sampling. We observe a slight over estimate of power in the simulations for scales smaller than $k = 3.0 h\text{Mpc}^{-1}$. This is caused by a known loss of accuracy in the predictions, as one progresses deep in the non-linear regime.

are observed in most N-body codes, and do not affect qualitatively the final results, as long as internal consistency is preserved.

In linear theory of structure formation, different Fourier modes of the matter density grow independently, such that the error bars on the power spectrum are well described by Gaussian statistics. For non-linear scales however, the phases of different Fourier modes start to couple together (Meiksin & White 1999; Coles & Chiang 2000; Chiang et al. 2002), hence the two-point function no longer contains all the information about the fields. Higher order statistics, i.e. bispectrum, trispectrum, are then needed in order to completely characterize the field. Theoretical calculations can describe these quantities with a reasonable accuracy in the translinear regime, but N-body simulations provide the most accurate estimates at all scales, as long as convergence is achieved. For a covariance matrix with N^2 bins, one needs *at least* the same amount of simulations. Our plan is to organize the lensing estimators in about ten bins, hence 185 simulations are enough. We recall here that the simulations described in this paper are primarily used to estimate the non-Gaussian covariance matrices of various weak lensing estimators, hence it is essential to pin down the source non-Gaussian features, and to monitor how these propagate in our calculations.

The power spectrum covariance matrix is defined as

$$C(k, k') = \langle P(k) - \bar{P}(k) \rangle \langle P(k') - \bar{P}(k') \rangle \quad (14)$$

where the over-bar refers to the best estimate of the mean. The amount of correlation between different scales is bet-

⁸ The version of HALOFIT that was used in our calculations does not incorporate recent corrections that were made in December 2011

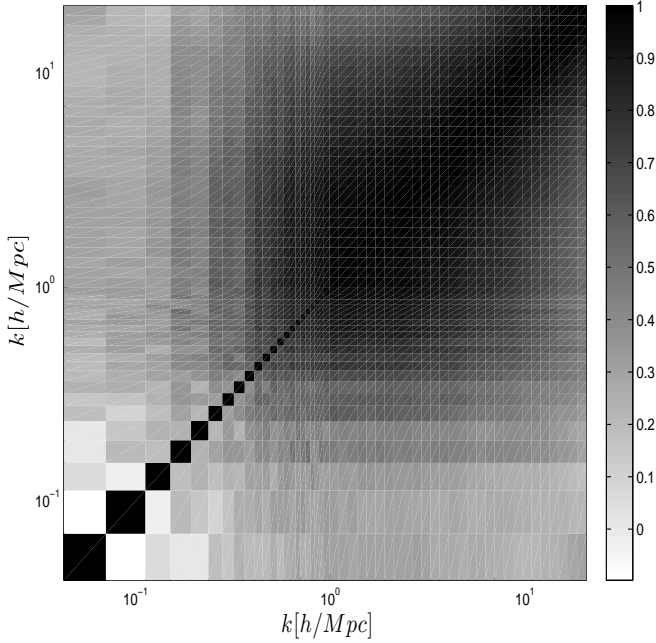


Figure 3. Normalized covariance matrix of the density power spectrum, measured from 185 N-body simulations, at redshift of 0.961. Modes at $k \sim 0.5 h\text{Mpc}^{-1}$, corresponding to $\theta \sim 18.35$ arcmin, are more than 40 per cent correlated.

ter visualized with the cross-correlation coefficient matrix, which is obtained from $C(k, k')$ via

$$\rho(k, k') = \frac{C(k, k')}{\sqrt{C(k, k)C(k', k')}} \quad (15)$$

and is shown for $z = 0.961$ in Fig. 3. We see that it is almost diagonal in larger scales (lower k), while measurements become correlated as we progress towards smaller scales (higher k). At $k \sim 0.5 h\text{Mpc}^{-1}$, for instance, the Fourier modes are intrinsically more than 40 per cent correlated. This corresponds to an angle of $\theta \sim 18.35$ arcmin on the sky, and $\ell \sim 1180$.

We stress that this correlation is intrinsic to the density fields, and that extracting this covariance matrix from an actual galaxy survey is a delicate task. Recent results have shown that neglecting either the non-Gaussian nature of the uncertainty, or the survey selection function can significantly underestimate the error on the power spectrum, even at scales traditionally considered as linear (Ngan et al. 2011; Harnois-Deraps & Pen 2011).

4.2 Angular Power

In order to quantify the resolution of our lensing maps, we measure the angular power spectrum of the $\kappa(\theta)$ fields, and compare the results with the non-linear predictions from Smith et al. (2003). The power spectrum of the convergence field is defined as:

$$\langle \kappa(\ell_1) \kappa(\ell_2) \rangle = (2\pi)^2 \delta_D(\ell_1 + \ell_2) P_\kappa(\ell_1) \quad (16)$$

where ℓ is the Fourier component corresponding to the real space vector θ . and where, again, the angle brackets refer to an angle average. The convergence power spectrum, esti-

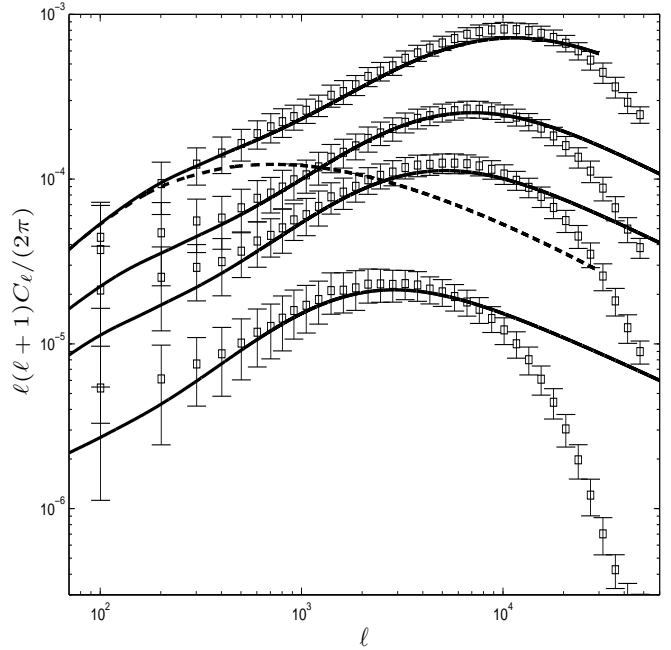


Figure 4. Convergence power spectrum, measured from 185 N-body simulations, where the source redshift distribution is a Dirac delta function at $z \sim 3.0, 1.5, 1.0$ and 0.5 (top to bottom symbols). The solid lines correspond to the non-linear predictions (Seljak & Zaldarriaga 1996), the linear prediction at $z_s = 3$ is represented by the dashed line, and the error bars are the 1σ standard deviation over our sampling. We observe a slight overestimate of power in the simulations for $z = 3$ and $\ell > 1000$ compared to non-linear predictions (solid line), and a more important bias for lower redshifts. This roots in the lack of predicted power which is also visible in the smallest scales of the three dimensional dark matter power spectrum (i.e. Fig. 2). Similar trends are observed in the Coyote Universe and SUNGLASS simulation suites. The low- ℓ power seems also to be in excess in the simulations, however predictions are still with the error bars.

mated from our simulations, is shown in Fig. 4 where the error bars are the 1σ standard deviation on the sampling. It is presented in the dimensionless form, i.e. $\ell(\ell+1)/(2\pi)P_\kappa(\ell)$ ⁹, which has the advantage of showing clearly which angles (or multipoles) are probing the linear regime. When compared with the non-linear theoretical model, we find a good agreement in the linear regime, while the theoretical predictions slightly underestimate the power for $\ell > 1000$, consistent with the observations of Hilbert et al. (2009). The strong drop at $\ell \sim 30000$ is caused by limitations in the resolution, which corresponds to an angle of about 0.7 arcmin.

As mentioned earlier, the smallest angles of weak lensing observations are probing the non-linear regime of the underlying density field, and it is known that the statistics describing the uncertainty on the weak lensing power spectrum are non-Gaussian (Doré et al. 2009). Although most of the departures from Gaussianity in the data are currently lost in the observation noise, future lensing surveys are expected to improve enough on statistics and systematics such that non-Gaussian features will become significant. The non-

⁹ In this paper, we use two notations interchangeably to denote the convergence angular power spectrum : $P_\kappa(\ell)$ and C_ℓ .

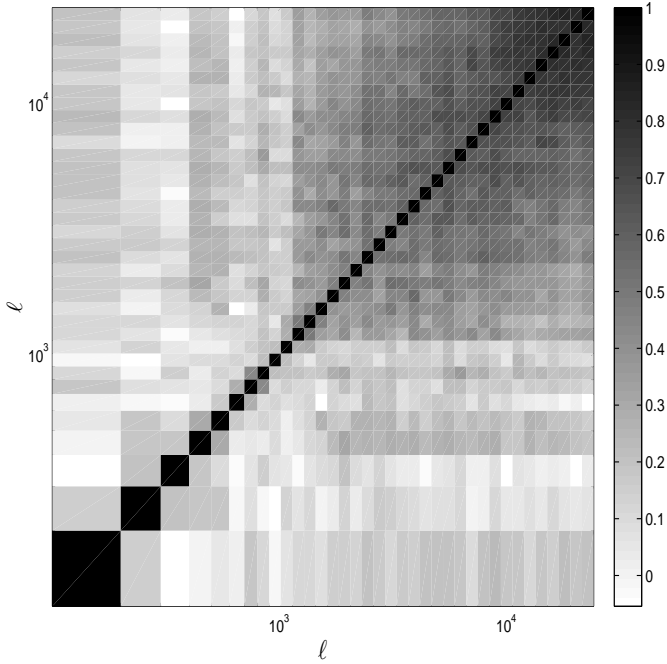


Figure 5. Cross-correlation coefficient matrix of the (dimension-full) convergence power spectrum, measured from 185 LOS. We observe a strong correlation for ℓ of a few thousand.

linear dynamics effectively correlate the error bars in small scales, as seen in Fig. 5. As expected, we observe that all the multipoles with $\ell > 1000$ are more than 40 per cent correlated.

5 2-POINT CORRELATION FUNCTIONS

Detection of a robust weak lensing signal from the data is a challenging task in itself, for many secondary effects need to be filtered out. The 2- and 3-point functions of the observed matter field are known to provide a wealth of information about the lensing signal. Generally, different statistical estimators and filtering techniques are sensitive to different scales, systematics and secondary effects, and correlate the measurements in a unique way.

It was recently shown (Vafaei et al. 2010) that the optimal approach for measurements involving the cosmic shear and convergence depends on the survey geometry and the cosmological parameters investigated. For instance, the shear 2-point correlation function minimizes the correlation across different angles, while the mass aperture window statistics correlate different angular scales even in the absence of signal. However, the latter has the advantage of being more sensitive to smaller scales, hence it is better suited for surveys of limited coverage (Schneider et al. 1998). In the following two sections, we give a short overview of the most commonly used statistical estimators and present their signal as detected in the simulations, compared to non-linear predictions.

As mentioned in section 2, the N-body simulations serve to construct the convergence and shear maps from the density fields. To mimic the actual detection from a galaxy survey, we Poisson sample each of the maps with 100000 ran-

dom points and construct mock catalogues, from which we extract the 2-point correlation function measurements. The positions are purely random within the 12.84 deg^2 patches, and the values at each point are interpolated from the simulated grids. This completely bypasses the galaxy population algorithm, which will be addressed in future work.

5.1 Shear

In current cosmic shear analyses, one of the strongest weak lensing signal comes from a measurement of the 2-point correlation function in the shear of galaxy, which is defined as:

$$\xi_{ij}(\theta) \equiv \langle \gamma_i(\theta') \gamma_j(\theta + \theta') \rangle \quad (17)$$

where i and j refer to a pair of galaxies separated by angle $\theta = |\theta|$. In the absence of gravitational lenses, $\xi_{ij}(\theta)$ averages out to zero, hence a positive signal indicates a detection of cosmic shear.

Since the intrinsic distortion produced by a single massive object is exclusively aligned in the tangential direction around the center of mass, it is possible to improve the lensing measurement by considering a local coordinate system, in which the *tangential* and *rotated* axes are defined as the direction perpendicular and parallel to the line joining two galaxies. The new, local, complex shear can be written as $\gamma = \gamma_t + i\gamma_r$, where t and r refer to tangential and radial shear respectively. The corresponding correlation function ξ_{tt} and ξ_{rr} are defined as the weighted average of the tangential and rotated shears for pairs of galaxies separated by an angle $\theta = |x_i - x_j|$, namely:

$$\xi_{tt} = \frac{\sum w_i w_j \gamma_t(x_i) \gamma_t(x_j)}{\sum w_i w_j} \quad (18)$$

$$\xi_{rr} = \frac{\sum w_i w_j \gamma_r(x_i) \gamma_r(x_j)}{\sum w_i w_j} \quad (19)$$

where the w_i refers to weights of objects i, j , which quantifies how well the corresponding shear is measured. The combination of tangential and rotated shear leads to $\xi_{\pm}(\theta)$:

$$\xi_{\pm}(\theta) = \xi_{tt} \pm \xi_{rr} \quad (20)$$

which are conveniently related to the convergence power spectrum:

$$\xi_{+}(\theta) = \int_0^{\infty} \frac{d\ell}{2\pi} \ell P_{\kappa}(\ell) J_0(\ell\theta) \quad (21)$$

$$\xi_{-}(\theta) = \int_0^{\infty} \frac{d\ell}{2\pi} \ell P_{\kappa}(\ell) J_4(\ell\theta) \quad (22)$$

where $J_n(x)$ is the n th order first kind Bessel function. Hence measurements of $\xi_{rr,tt}$ give a direct handle on many cosmological parameters that depend on $P_{\kappa}(\ell)$, (seven in total, but mainly σ_8 and Ω_m).

We show in Fig. 6 and 7 the 2-point correlation functions ξ_{tt} and ξ_{rr} respectively, as a function of the separation angle and for 4 different redshifts. The error bars are the 1σ standard deviation as obtained from our 185 lines of sight. The agreements between the simulations and the theoretical predictions are well within the error bars down to 0.6 arcmin, which allows us to conclude that the signals are well resolved at least in that range.

We next show in Fig. 8 the cross-correlation coefficient

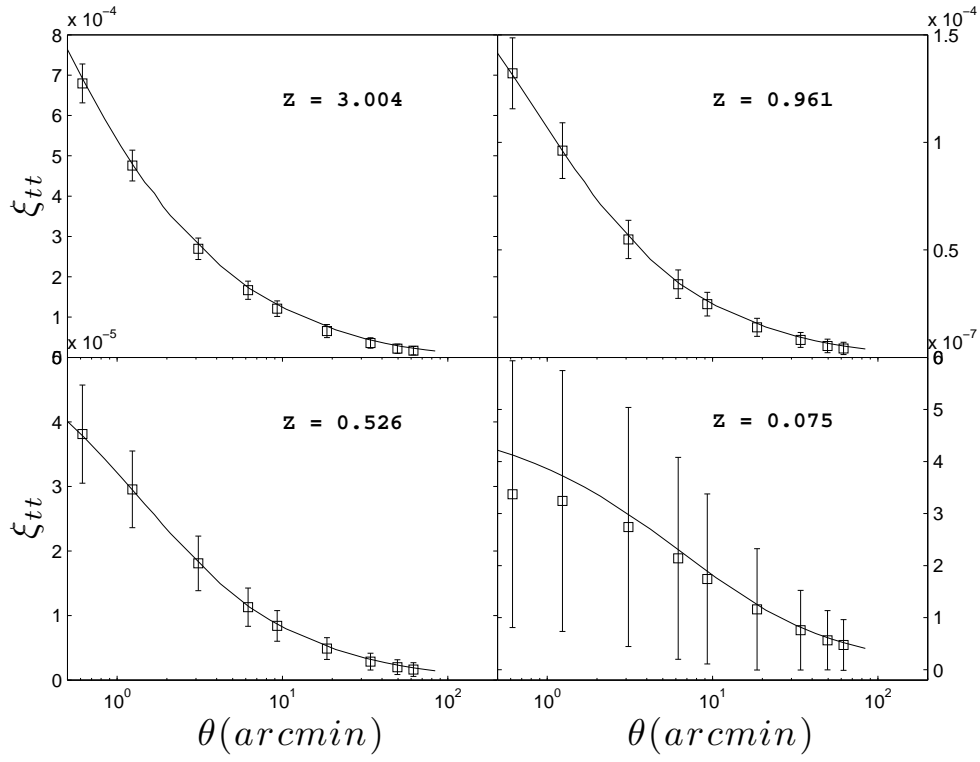


Figure 6. Shear correlation function ξ_{tt} , computed from Poisson sampling the simulated shear maps in the local (tt, rr) coordinates, as described in the text. The solid line shows non-linear theoretical predictions on the mean of the estimators.

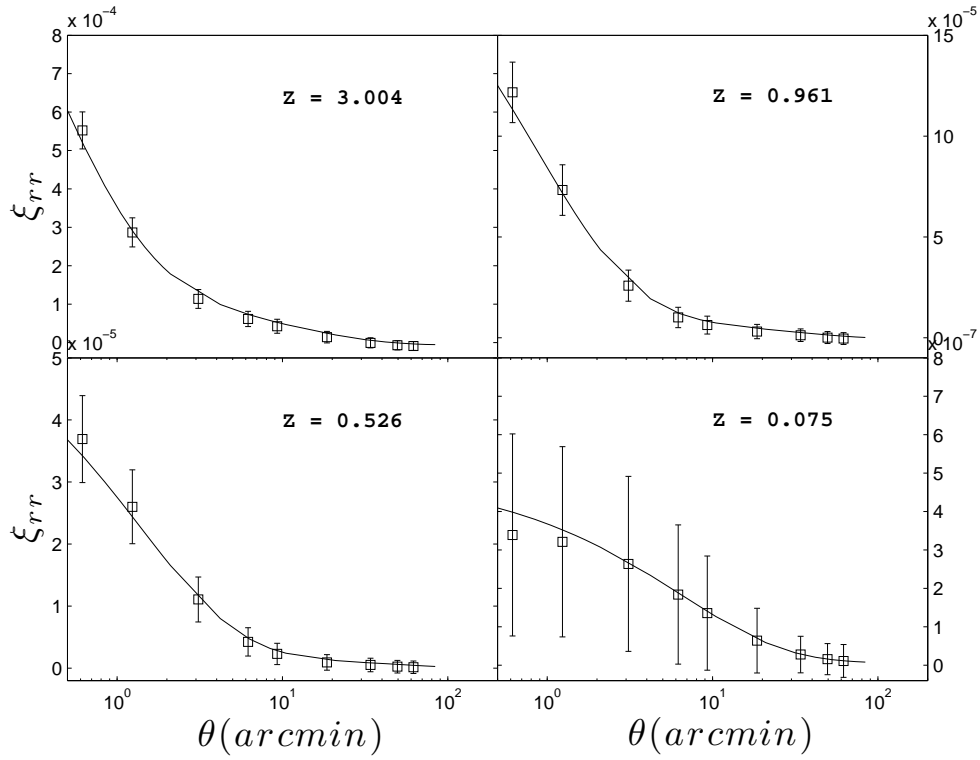


Figure 7. ξ_{rr} component.

matrices related to the tt measurements, for source redshifts of 3.0 and 1.0. These show that the error bars across different angles are at least 50 per cent correlated for the highest redshift, and up to 80 per cent for lower redshift sources. This correlation becomes even stronger as the two angles become similar in size. The rr matrices are qualitatively similar, hence we do not show them here.

5.2 Convergence

Convergence – or magnification – signal has been successfully detected in recent analyses (Scranton et al. 2005; Hildebrandt et al. 2009, 2011). Although more challenging to detect in the data, it is worth the effort, first as it serves as a cross-check of the shear results, and second as it is theoretically cleaner: no (non-local) Fourier transforms are needed in the process of map construction. Following the procedure developed for the shear fields, we calculate the two-point $\kappa - \kappa$ correlation function from the Poisson sampling of the simulated convergence maps. In Fig. 9, we present our results, compared with the non-linear theoretical predictions, and find that the agreement extends deep under the arc minute at all redshifts as well.

We have also measured the cross-correlation coefficient matrices corresponding to these measurements, and because they are very similar to the γ_{tt} matrices, we do not present the matrices here, but make them available upon request.

6 WINDOW-INTEGRATED CORRELATION FUNCTIONS

As briefly explained earlier, depending on the survey, the 2-point correlation functions are not always the best way to measure the cosmic shear or convergence. Window-integrated correlation functions, such as the mass aperture variance, give a second handle on many cosmological parameters (Schneider et al. 1998), and are also used in galaxy-galaxy lensing and cluster lensing. Generally, the method consists in measuring the mean, the variance or even higher-order statistics of a given lensing field, which was beforehand convolved with either a ‘top hat’ or a compensated filter of variable smoothing angle θ . The integrated results are computed as a function of the smoothing angle, and can usually be compared with theoretical predictions for the lensing power spectrum.

When extracting this kind of estimator on the shear signal, the choice of filter matters. One of the advantage of the top hat filter is that it probes scales as large as the field of view, whereas compensated filters are limited by a damping tail in the window shape that prevents using the boundaries of the patch. Another advantage of the top hat filter is that it yields a signal to noise that is optimal for a skewness measurement (Vafaei et al. 2010). On the other hand, a compensated mass aperture filter is more sensitive to smaller scales, hence it does a better job at recovering signal on surveys with smaller area. In addition, it is measured directly from the tangential shear field (Kaiser & Squires 1993; Schneider 1996), hence is not affected by the systematic and statistical uncertainties involved in the reconstruction of the convergence field. For these reasons, different analyses will prefer

different estimator, hence we consider both kinds of filters for completeness.

The top hat filter is a circular aperture of radius θ , outside of which the signal is cut to zero. The filtering process effectively measures the total shear in a filtered region of a map, $\bar{\gamma}$, for a given opening angle θ . We repeat such measurement over many patches on each map and measure the top hat variance $\langle |\bar{\gamma}|^2 \rangle_{TH}$, which is related to the convergence power spectrum P_κ as:

$$\langle |\bar{\gamma}|^2(\theta) \rangle_{TH} = \frac{1}{2\pi} \int d\ell \ell P_\kappa(\ell) W_{TH}(\ell\theta) \quad (23)$$

with $W_{TH}(\ell\theta) = \frac{4J_1^2(\ell\theta)}{(\ell\theta)^2}$ (Kaiser 1992). This convolution process is done with Fourier transforms, and each of the maps are zero-padded in order to reduce the effect of boundaries. We compare our measurements from the simulations with non-linear predictions in Fig. 10, as a function of the opening angle of the top hat filter, and find a good agreement at all redshift, although $z = 0.075$ exhibits a small positive bias. The cross-correlation matrices are presented in Fig. 11 and show that there is a strong correlation between most measurements.

We next consider a compensated aperture filter, which is constructed from the local tangential shear in mock catalogues, where the role of the central galaxy in the pair counting is played by the centre of the filter. The aperture mass M_{ap} is then given by (Schneider et al. 1998):

$$M_{ap}(\theta) = \int d^2\vartheta Q_\theta(\vartheta) \gamma_t(\vartheta) \quad (24)$$

where Q is a weight function with support $|\vartheta| \in [0, \theta]$ and which takes the shape:

$$Q_\theta(\vartheta) = \frac{6}{\pi\theta^2} \left(\frac{\vartheta}{\theta^2} \right) \left(1 - \frac{\vartheta^2}{\theta^2} \right) \quad (25)$$

We then calculate the variance $\langle M_{ap}^2 \rangle$ across the map, for all available angles, which is also related to the convergence power spectrum P_κ by:

$$\langle M_{ap}^2(\theta) \rangle = \frac{1}{2\pi} \int_0^\infty d\ell \ell P_\kappa(\ell) W_{ap}(\ell\theta) \quad (26)$$

where $W_{ap}(\ell\theta) = \frac{276J_2^2(\ell\theta)}{(\ell\theta)^4}$. We present in Fig. 12 our measurements of $\langle M_{ap}^2 \rangle$ from the simulations, as a function of smoothing scale θ . Over plotted are the theoretical predictions obtained from [Eq. 26] with a non-linear convergence power spectrum. We observe that for redshifts larger than one, the agreement extends down to the arc minute, whereas lower redshifts suffer from a lack of variance at angles of a few arc minutes. This is caused by limitations in the resolution due to strong zooming from the simulation grid on to the pixel map. We recall that an aperture mass is constructed with a compensated filter, which has a strong damping tail, hence for an opening angle θ , it is really sensitive to $\sim \theta/5$. This thus approaches simulation resolution at very low redshifts. This drop is also expected from the top hat variance, but appears at much smaller smoothing angles. The cross-correlation coefficient matrices are presented in Fig. 13, and show that most measurements are close to 60 per cent correlated. The smallest angles probe scales that are approaching the pixel resolution, hence there is very little cross-correlation.

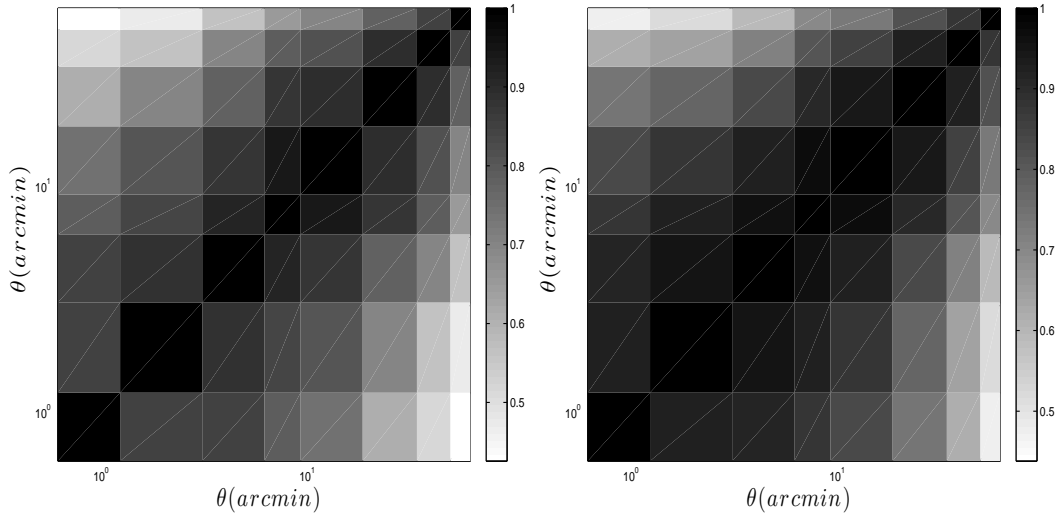


Figure 8. Cross-correlation coefficient matrix of the tt two-point function, with the source plane at $z \sim 3.0$ (left) and $z \sim 1.0$ (right).

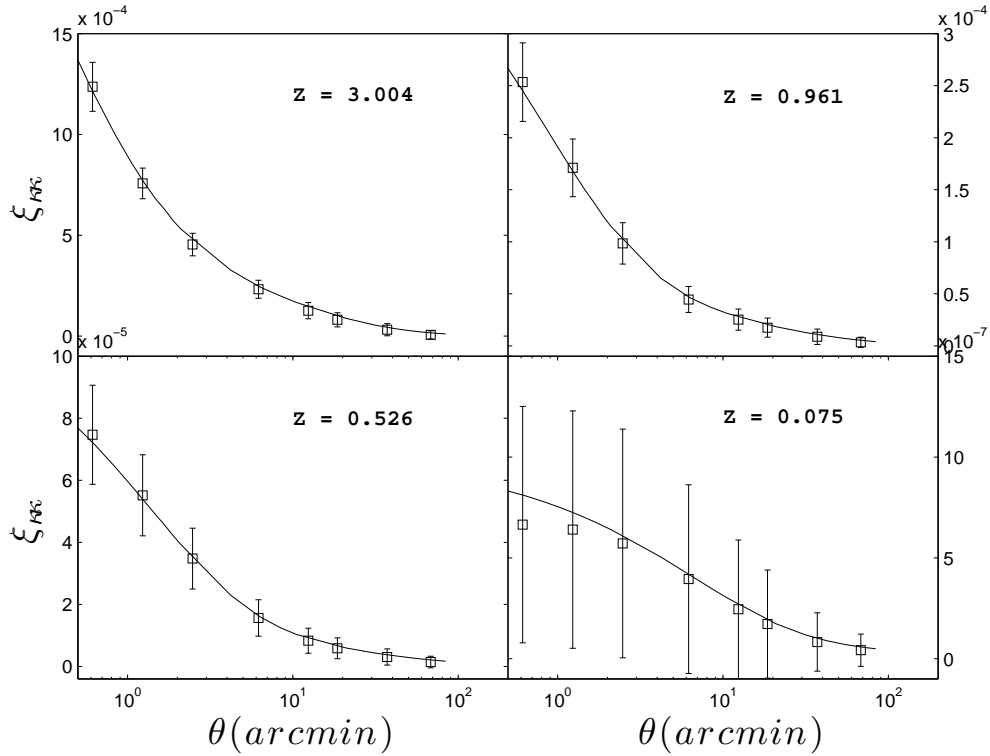


Figure 9. Convergence correlation function $\xi_{\kappa\kappa}$, at four different redshifts, constructed from Poisson samplings of the simulated maps. The error bars are the 1σ standard deviation in the 185 realizations.

7 WINDOWED STATISTICS ON CONVERGENCE MAPS

Window statistics performed directly on the convergence fields serve as an important test of the accuracy and precision of the simulations, since the calculations here can be done directly on the grid, i.e. without the Poisson sampling. We smooth the κ -maps with filters identical to those used in the last section and proceed to calculate the top hat variance $\langle \bar{\kappa}^2(\theta) \rangle_{TH}$ and mass aperture variance $\langle M_{ap}^2(\theta) \rangle$ as a

function of the filter opening angle. In the latter case, the choice of compensated filter (i.e. the equivalent of $Q_\theta(\vartheta)$ in [Eq. 25]) is given by $U_\theta(\vartheta)$ (Schneider et al. 1998), where:

$$U_\theta(\vartheta) = \frac{9}{\pi\theta^2} \left(1 - \frac{\vartheta}{\theta^2}\right) \left(\frac{1}{3} - \frac{\vartheta^2}{\theta^2}\right) \quad (27)$$

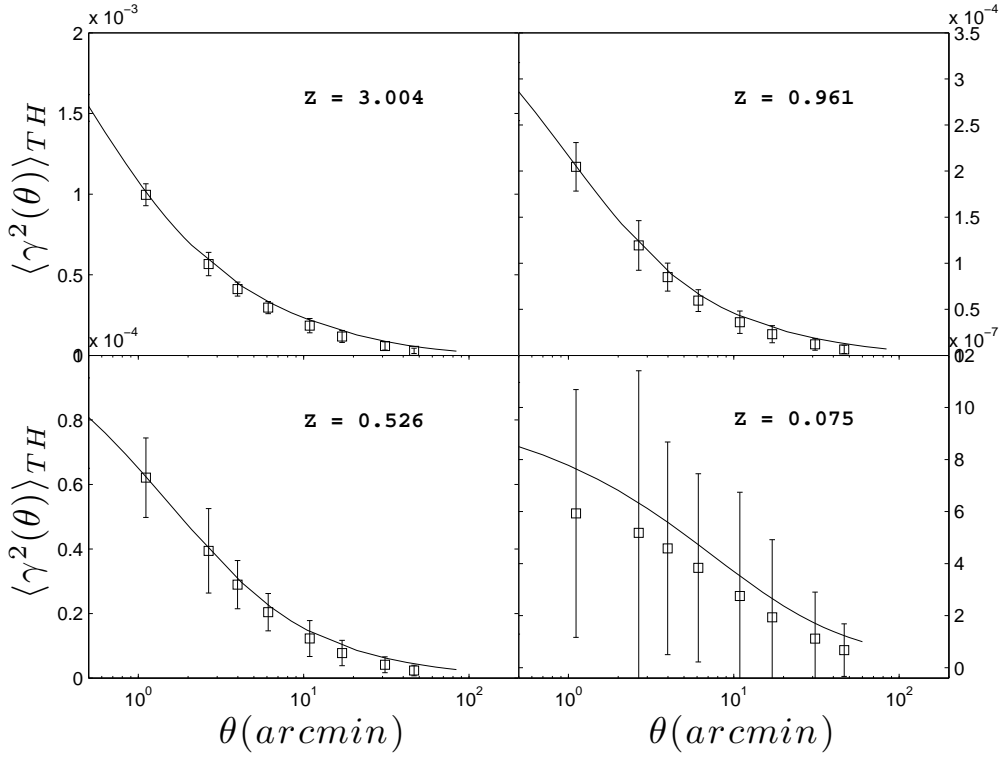


Figure 10. Top hat variance, $\langle |\bar{\gamma}|^2 \rangle$, measured from shear maps, for 4 different redshifts.

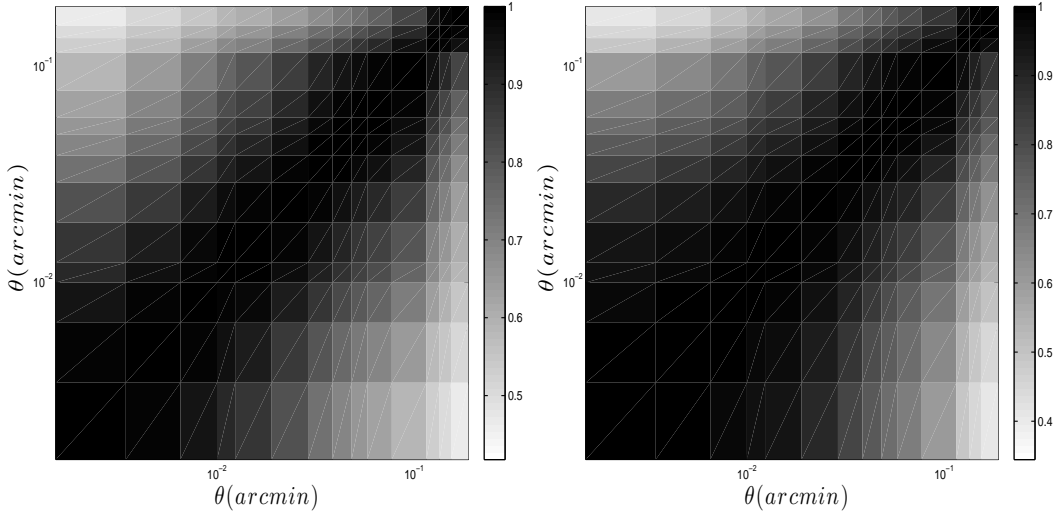


Figure 11. Cross-correlation coefficient matrix of the top hat variance, with the source plane fixed at $z \sim 3.0$ (left) and $z \sim 1.0$ (right).

In analogy to [Eq. 24], the M_{ap} estimator that is obtained from the convergence maps is calculated as:

$$M_{ap}(\theta) = \int d^2\vartheta U_{\theta}(\vartheta) \kappa(\vartheta) \quad (28)$$

We present in Fig. 14 and 15 the comparison with non-linear predictions, and observe a signal that is almost identical with the corresponding shear estimator. Namely, the agreement is good at all redshifts for the top hat variance, with only a slight bias at the lowest redshifts, whereas the mass aperture variance shows a lack of signal at angles of a few

arc minutes for low redshifts. Once again, this comes as no surprise since this approaches the grid size.

We also show the three-point function $\langle M_{ap}^3(\theta) \rangle$ and $\langle \bar{\kappa}^3(\theta) \rangle_{TH}$ in Fig. 16 and 17, which allow to break the degeneracy between σ_8 and Ω_m . We observe that our simulations tend to overestimate the mass aperture predictions by 1σ at low angles. This comes again from the fact that the aperture filter is sensitive to about one fifth of the total opening angle probed. Hence the discrepancy observed at $\theta \sim 2$ arcmin is

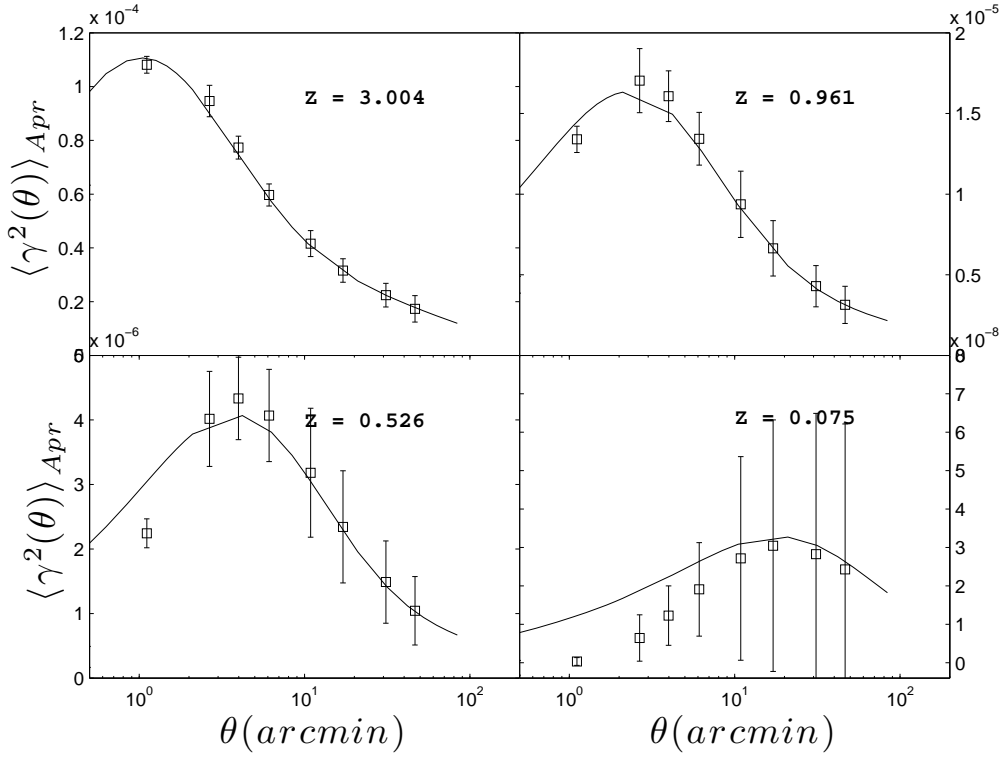


Figure 12. Aperture mass variance (M_{ap}^2) measured from shear maps. The apparent discrepancy between simulations and theoretical predictions at low redshift is caused by resolution limits, where the small angles actually probe scales that are very close to the grid size. The intrinsic pixel size of 0.21 arcmin has effects up to scales of about 1.0 arcmin.

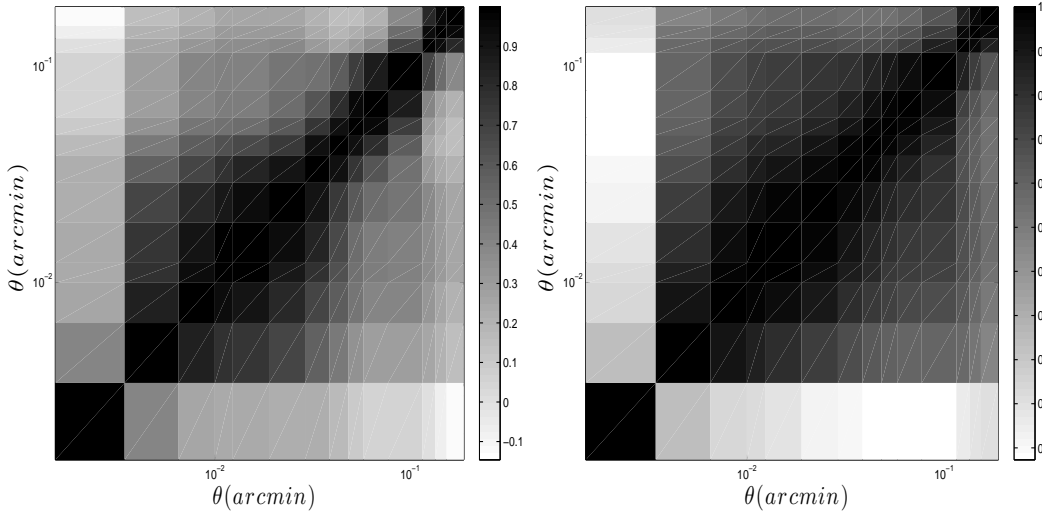


Figure 13. Cross-correlation coefficient matrix of the aperture window integrated shear, with the source plane at $z \sim 3.0$ (left) and $z \sim 1.0$ (right). The correlation seems to vanish in the first bin, however, for reasons discussed in the text, these bins are under-resolved, hence the largest modes.

mainly probing scales of 0.4 arcmin, which is of the order of the pixel size.

8 HALO CATALOGUES

This section briefly describes how the halo catalogues are created, and presents a few of the properties that are extracted on individual objects. We recall that our is to construct mock galaxy catalogues on which many secondary effects will be quantified. As mentioned be-

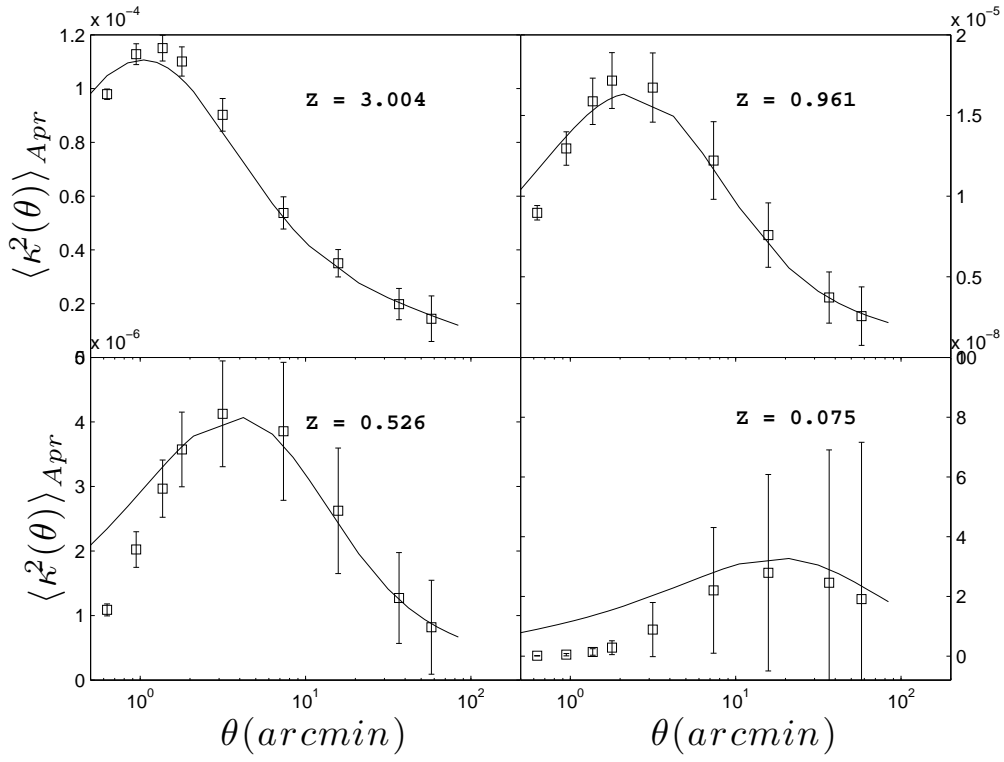


Figure 14. Aperture mass variance $\langle M_{ap}^2 \rangle$, measured directly from the convergence maps. We recall that the effect of finite pixel size is felt to larger angular scales – up to about one arc minute – with this estimator.

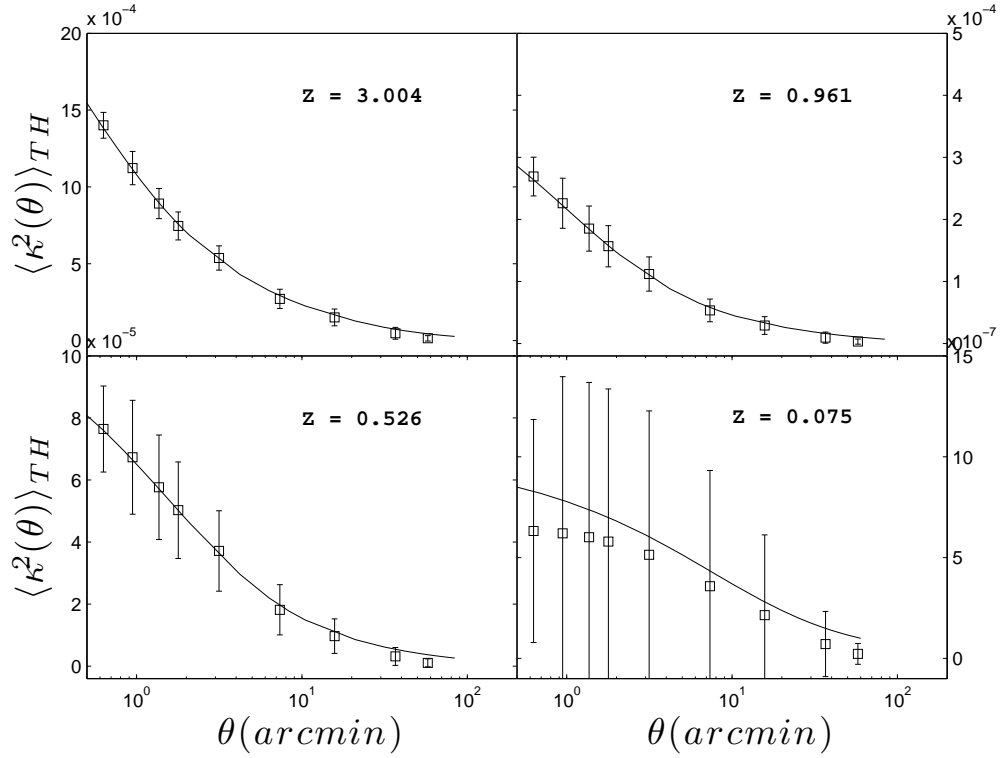


Figure 15. $\langle |\bar{\gamma}|^2 \rangle_{TH}$ measured directly from the convergence maps. We see that the agreement is excellent at all redshifts.

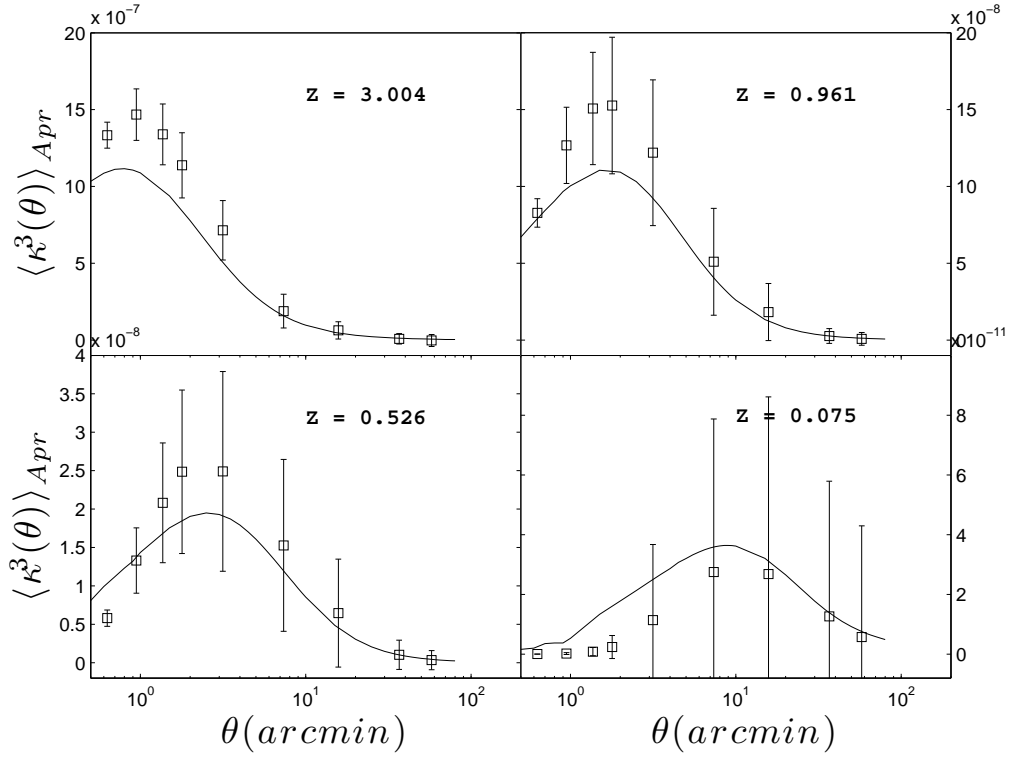


Figure 16. $\langle M_{ap}^3 \rangle$ measured directly from the convergence maps. We recall that the effect of finite pixel size is felt to larger angular scales – up to about one arc minute in lower redshift lenses – with this estimator, which explains the damped tail at small angles in the $z = 0.075$ plot.

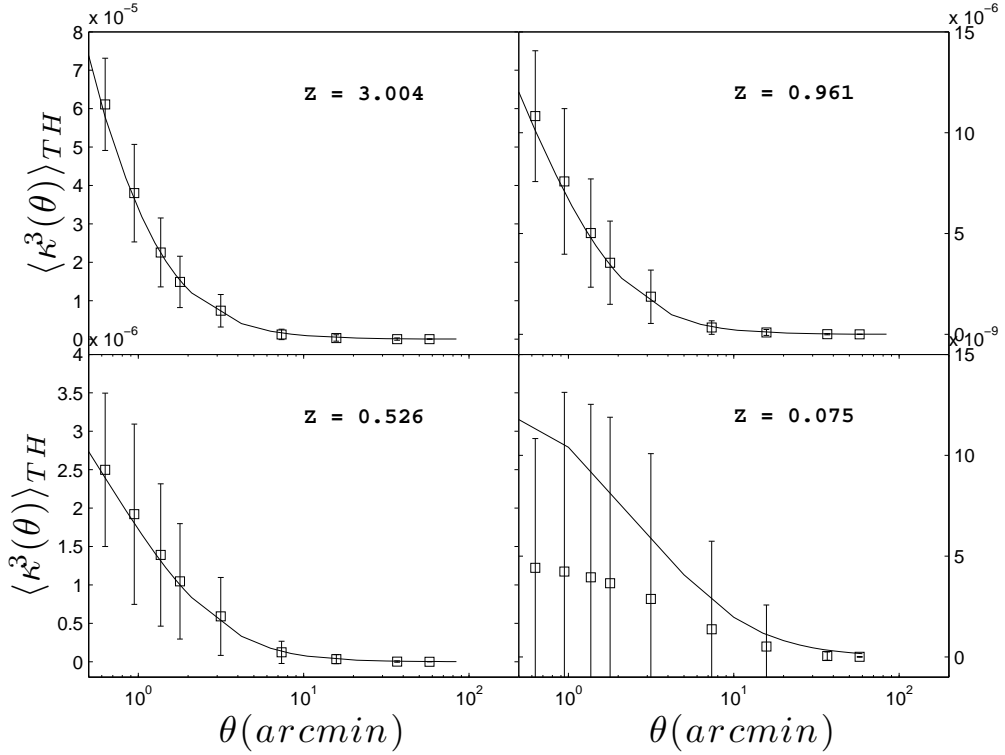


Figure 17. $\langle |\bar{\gamma}|^3 \rangle_{TH}$ measured directly from the convergence maps.

fore, we do not attempt to populate the haloes in this paper, since this is a challenge on its own, and we wish to factor out this problem for now. In the future, though, one could follow (Heymans et al. 2006), and populate the haloes with galaxies under the conditional luminosity function of (Cooray & Milosavljević 2005), then assign ellipticity following the elliptical or spiral model (Heavens et al. 2000; Heymans et al. 2004). Alternatively, one could use the GALICS (Hatton et al. 2003) and MO-MAF (Blaizot et al. 2005) to create mock galaxy catalogues directly our halo catalogues, following the prescription described in (Forero-Romero et al. 2007). Our plan is to incorporate, for the first time and in a systematic way, the prescriptions for intrinsic alignment, source clustering, ellipticity-shear correlation, etc. (De Lucia & Blaizot 2007; Schneider & Bridle 2010) all at once. This is crucial in order to interpret correctly the signal from the data, which contains all these contributions.

In this work, haloes are constructed from the matter density fields with a spherical overdensity algorithm (Cole & Lacey 1996). The first step is to assign the dark matter particles on a 2048^3 grid with the Nearest Grid Point scheme (Hockney & Eastwood 1981), and identify local density maxima. The halo finder then ranks these halo candidates in decreasing order of peak height, and for those which are above an inspection threshold value, it grows a spherical volume centered on the peak, computing for each shell the integrated overdensity until it drops under the predicted critical value. The haloes that are analyzed first are then removed from the density field, in preparation for the inspection of lower mass candidates. This prevents particles from contributing multiple times, but at the same time limits the resolution on sub-structures of the largest haloes. This is a mild cost for the purpose of these catalogues, which are populated with low multiplicity of galaxies, and thus depend rather weakly on the sub-halo structures. Finally, for each halo, we measure the mass, the centre-of-mass (CM) and peak positions, the CM velocity, the velocity dispersion, the angular momentum in the CM frame, and the inertia matrix σ_{ij} , which allows us to assign galaxy population beyond the sole halo mass. Although the latter quantity is biased by the fact that we are only searching for spherical regions, we still recover enough information about the shape and orientation.

In all the plots presented in this section, we present properties of the haloes that populate the full simulation box, even though, in the final mock catalogues, we keep only those that sit inside the past light cone. We apply the coordinate rotation and the random shifting of the origin that was performed on the lensing slabs, such that the halo catalogues and the lenses trace the same underlying density field.

To quantify the accuracy of the halo catalogues, we first extract the power spectrum of the distribution, and compare the results with the measurements from dark matter particles by computing the halo bias, defined as $b(k) = \sqrt{P_{\text{halo}}(k)/P_{\text{particle}}(k)}$. From Fig. 18, we observe that both the shape and redshift dependence agree well with the results from Iliev et al. (2011). We observe in Fig. 19 that the halo mass function is in good agreement with Press & Schechter (1974) and Sheth & Tormen (2002) in the range $1 \times 10^{11} - 2 \times 10^{14} M_{\odot}$. Higher redshift seems to better

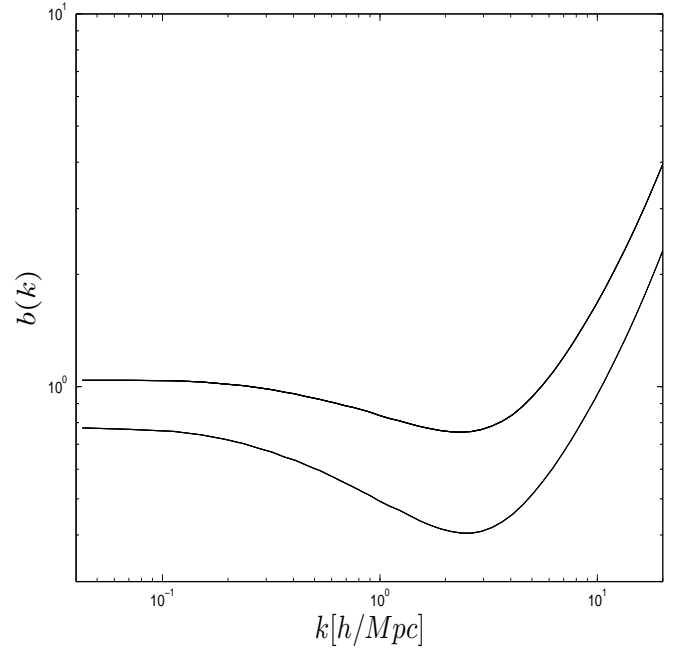


Figure 18. Halo bias, for redshifts 0.025 (bottom curve) and 0.961 (top curve).

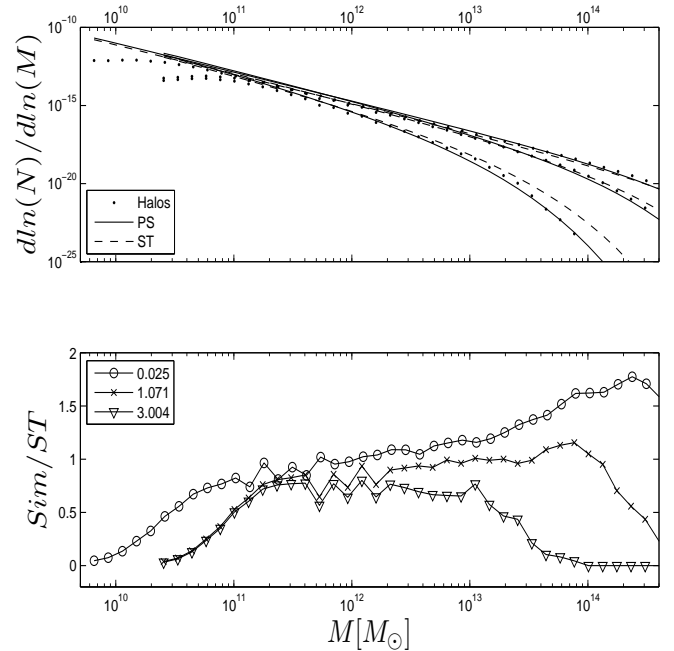


Figure 19. *top:* Halo mass function, compared to predictions, for redshift 0.025, 1.071 and 3.004 (top to bottom curves). *bottom:* Ratio of the mass function to the theoretical predictions of Sheth-Tormen.

fit Press-Schechter, while lower redshifts are better described by the Sheth-Tormen model.

We now present some of the relationships between the main kinematic quantities of these haloes. In Fig. 20, 21 and 22, we show, for $z = 0.025, 0.961$ and 3.004 respectively, and from top left to bottom right: the angular momentum L versus the mass m , the halo CM velocity v_{cm} versus m , L versus

v_{cm} , then the dispersion velocity v_{disp} versus m , L versus v_{disp} , and finally σ versus m , where σ is the angle average of the standard deviation on the centre of mass position. It is related to the inertia matrix via $\sigma^2 = \frac{1}{3} \sum_{i=1}^3 \sigma_{ij}^2$. The mass is in M_\odot , the velocity is in km s^{-1} , the distances in $h^{-1}\text{Mpc}$, and the angular momentum in $h^{-1}\text{Mpc km s}^{-1}$. The plots are bivariate histograms, arranged in 50x50 bins, and the color bars are in logarithm scale for higher contrasts.

9 CONCLUSION

This paper has two principal objectives: 1) measure accurate non-Gaussian covariance matrices at the sub-arcminute precision on the principal weak lensing estimators, and 2) set the stage for systematic studies of secondary effects, and especially how their combination impacts the lensing signal. We have generated a set of 185 high resolution N-body simulations from which we constructed past light cones with a ray tracing algorithm. The weak lensing signal is accurately resolved from a few degrees down to below the arc minute. Thanks to the large statistics, we have measured non-Gaussian error bars on a variety of weak lensing estimators, including 2-point correlation functions on shear and convergence, and window integrated estimators such as the mass aperture. In each case, we compared our results with non-linear theoretical predictions at a few redshifts and obtained a good agreement, which testifies the quality of the simulations. The extracted error bars are essential for a correct estimate of many lensing signals, including sensitivity to cosmological parameters, which so far relied on Gaussian assumptions, or on numerical estimates that were not resolving the complete dynamical range. With the next generation of lensing survey, non-Gaussian error bars are expected to deviate significantly from Gaussian prescriptions, therefore techniques such as those presented here will be required for robust estimates.

In addition, we measured the covariance matrices of these weak lensing estimators, and we show that the error bars between different angular measurements are at least 50 per cent correlated, with regions up to 90 per cent correlated, as the two angles become closer. This needs to be taken into account when propagating the non-Gaussian uncertainty from these estimates on to other parameters.

We also generated a series of halo mock catalogues that are coupled to the gravitational lenses constructed, for future independent studies of secondary signals and alternate testing of lensing estimators. Within the CFHTLenS collaboration, these catalogues will be part of the CLONE project. We finally present an overview some key kinematic variables in our halo catalogues, including the mass dependence of the velocity dispersion and of the angular momentum. Our near term goal is to include effects such as intrinsic alignment, source clustering, etc. in our galaxy population algorithm and quantify their combined contribution. In addition, we plan to quantify the impact of post-Born calculations on the non-Gaussian uncertainty and on the contamination by secondary signals. Understanding the impact of all these effects is essential, for such systematic bias are likely to contribute significantly to future surveys such as KiDS and EUCLID.

Aspects not included in our simulation settings are feedback effects (Semboloni et al. 2011) and dependence

of the covariance matrices on the cosmological parameters (Eifler et al. 2009). While the latter can be simply addressed by running additional simulations, the former necessitates the construction of hydrodynamical simulations that implement simultaneously matter clustering at large angular scales and a proper modelisation of feedback effects.

ACKNOWLEDGMENTS

The authors would like to thank Ue-Li Pen, Dmitri Pogosyan, Catherine Heymans, Fergus Simpson, Elisabetta Semboloni, Hendrick Hildebrandt, Martin Kilbinger and Christopher Bonnett for useful discussions and comments on the manuscripts. LVW acknowledges the financial support of NSERC and Cifar, and JHD is grateful for the FQRNT scholarship under which parts of this research was conducted. N-body computations were performed on the TCS supercomputer at the SciNet HPC Consortium. SciNet is funded by: the Canada Foundation for Innovation under the auspices of Compute Canada; the Government of Ontario; Ontario Research Fund - Research Excellence; and the University of Toronto.

REFERENCES

- Albrecht A., et al., 2006, ArXiv e-prints (astro-ph/060959)
- Bartelmann M., Schneider P., 2001, *Phys. Rep.*, 340, 291
- Beaulieu J. P., et al., 2010, in V. Coudé Du Foresto, D. M. Gelino, & I. Ribas ed., *Pathways Towards Habitable Planets* Vol. 430 of *Astronomical Society of the Pacific Conference Series*, EUCLID: Dark Universe Probe and Microlensing Planet Hunter. pp 266–
- Benjamin J., Heymans C., Semboloni E., van Waerbeke L., Hoekstra H., Erben T., Gladders M. D., Hettterscheidt M., Mellier Y., Yee H. K. C., 2007, *MNRAS*, 381, 702
- Bernardeau F., 1998, *A&A*, 338, 375
- Bernardeau F., Colombi S., Gaztañaga E., Scoccimarro R., 2002, *Phys. Rep.*, 367, 1
- Bernardeau F., van Waerbeke L., Mellier Y., 1997, *A&A*, 322, 1
- Blaizot J., Wadadekar Y., Guiderdoni B., Colombi S. T., Bertin E., Bouchet F. R., Devriendt J. E. G., Hatton S., 2005, *MNRAS*, 360, 159
- Blandford R. D., Saust A. B., Brainerd T. G., Villumsen J. V., 1991, *MNRAS*, 251, 600
- Chiang L.-Y., Coles P., Naselsky P., 2002, *MNRAS*, 337, 488
- Cole S., Lacey C., 1996, *MNRAS*, 281, 716
- Coles P., Chiang L., 2000, *Nature*, 406, 376
- Coles P., Jones B., 1991, *MNRAS*, 248, 1
- Colless M., et al., 2003, ArXiv e-prints (astro-ph/0306581)
- Cooray A., Milosavljević M., 2005, *ApJ*, 627, L89
- Cooray A., Sheth R., 2002, *Phys. Rep.*, 372, 1
- De Lucia G., Blaizot J., 2007, *MNRAS*, 375, 2
- Doré O., Lu T., Pen U.-L., 2009, ArXiv e-prints
- Eifler T., Schneider P., Hartlap J., 2009, *A&A*, 502, 721
- Eisenstein D. J., et al., 2005, *ApJ*, 633, 560
- Forero-Romero J. E., Blaizot J., Devriendt J., van Waerbeke L., Guiderdoni B., 2007, *MNRAS*, 379, 1507
- Harnois-Deraps J., Pen U.-L., 2011, ArXiv e-prints

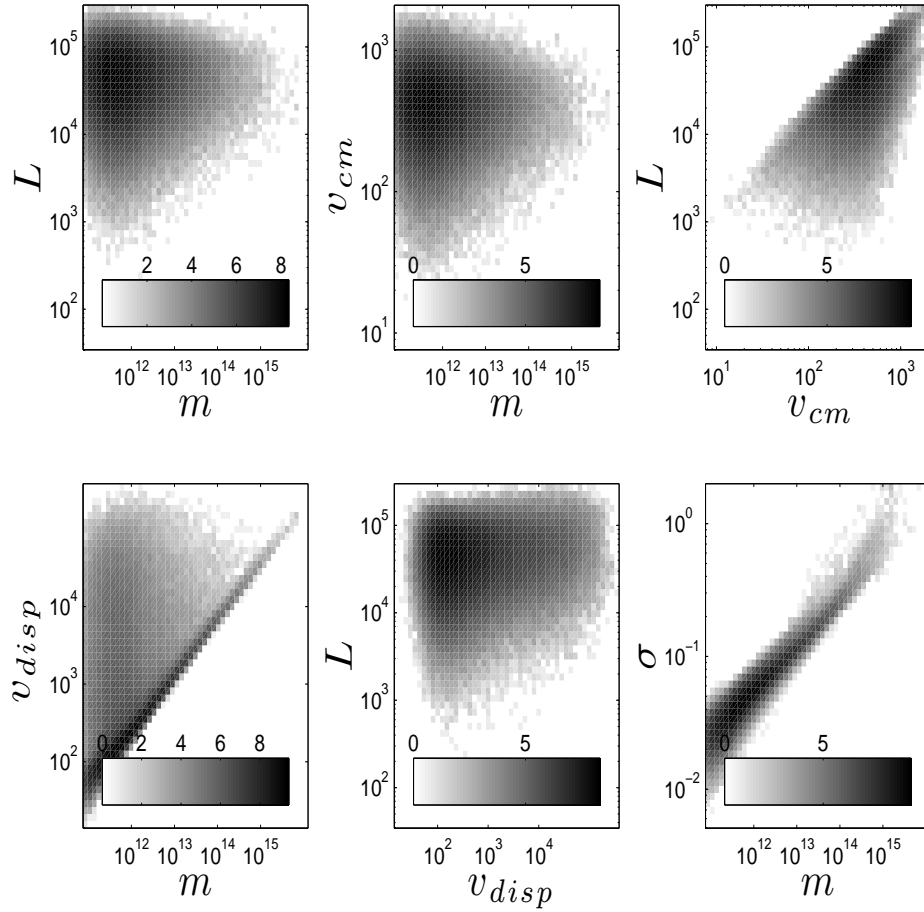


Figure 20. Halo properties at $z=0.025$. *top, from left to right:* L vs. m , v_{halo} vs. m and L vs. v_{halo} . *bottom, from left to right:* v_{disp} vs. m , L vs. v_{disp} and σ vs. m . See the text for definitions of these quantities. The mass is in M_{\odot} , the velocity is in km s^{-1} , the distances in $h^{-1}\text{Mpc}$, and the angular momentum in $h^{-1} \text{Mpc km s}^{-1}$. The plots are bivariate histograms, where the haloes in the catalogue were binned and counted according to the kinematical properties under study.

Hatton S., Devriendt J. E. G., Ninin S., Bouchet F. R., Guiderdoni B., Vibert D., 2003, MNRAS, 343, 75
 Heavens A., Peacock J., 1988, MNRAS, 232, 339
 Heavens A., Refregier A., Heymans C., 2000, MNRAS, 319, 649
 Heymans C., Brown M., Heavens A., Meisenheimer K., Taylor A., Wolf C., 2004, MNRAS, 347, 895
 Heymans C., White M., Heavens A., Vale C., van Waerbeke L., 2006, MNRAS, 371, 750
 Hilbert S., Hartlap J., White S. D. M., Schneider P., 2009, A&A, 499, 31
 Hildebrandt H., Muzzin A., Erben T., Hoekstra H., Kuijken K., Surace J., van Waerbeke L., Wilson G., Yee H. K. C., 2011, ApJ, 733, L30
 Hildebrandt H., van Waerbeke L., Erben T., 2009, A&A, 507, 683
 Hirata C. M., Seljak U., 2004, Phys. Rev. D, 70, 063526
 Hockney R. W., Eastwood J. W., 1981, Computer Simulation Using Particles
 Hoekstra H., Jain B., 2008, Annual Review of Nuclear and Particle Science, 58, 99
 Huterer D., 2002, Phys. Rev. D, 65, 063001
 Iliev I. T., Mellema G., Shapiro P. R., Pen U.-L., Mao Y.,

Koda J., Ahn K., 2011, ArXiv e-prints
 Jain B., Seljak U., White S., 2000, ApJ, 530, 547
 Jarosik N., et al., 2011, ApJS, 192, 14
 Kaiser N., 1992, ApJ, 388, 272
 Kaiser N., Squires G., 1993, ApJ, 404, 441
 Kiessling A., Heavens A. F., Taylor A. N., Joachimi B., 2011, MNRAS, 414, 2235
 Kiessling A., Taylor A. N., Heavens A. F., 2011, MNRAS, 416, 1045
 Komatsu E., et al., 2011, ApJS, 192, 18
 Krause E., Hirata C. M., 2010, A&A, 523, A28
 Lawrence E., Heitmann K., White M., Higdon D., Wagner C., Habib S., Williams B., 2010, ApJ, 713, 1322
 Lazio J., 2008, in R. Minchin & E. Monjjan ed., The Evolution of Galaxies Through the Neutral Hydrogen Window Vol. 1035 of American Institute of Physics Conference Series, The Square Kilometer Array. pp 303–309
 Lee J., Pen U.-L., 2008, ApJ, 686, L1
 Limber D. N., 1953, ApJ, 117, 134
 Loken C., et al., 2010, J. Phys.: Conf. Ser., 256, 1
 LSST Science Collaborations et al., 2009, ArXiv e-prints (astro-ph/0912.0201)
 Lu T., Pen U.-L., Doré O., 2010, Phys. Rev. D, 81, 123015

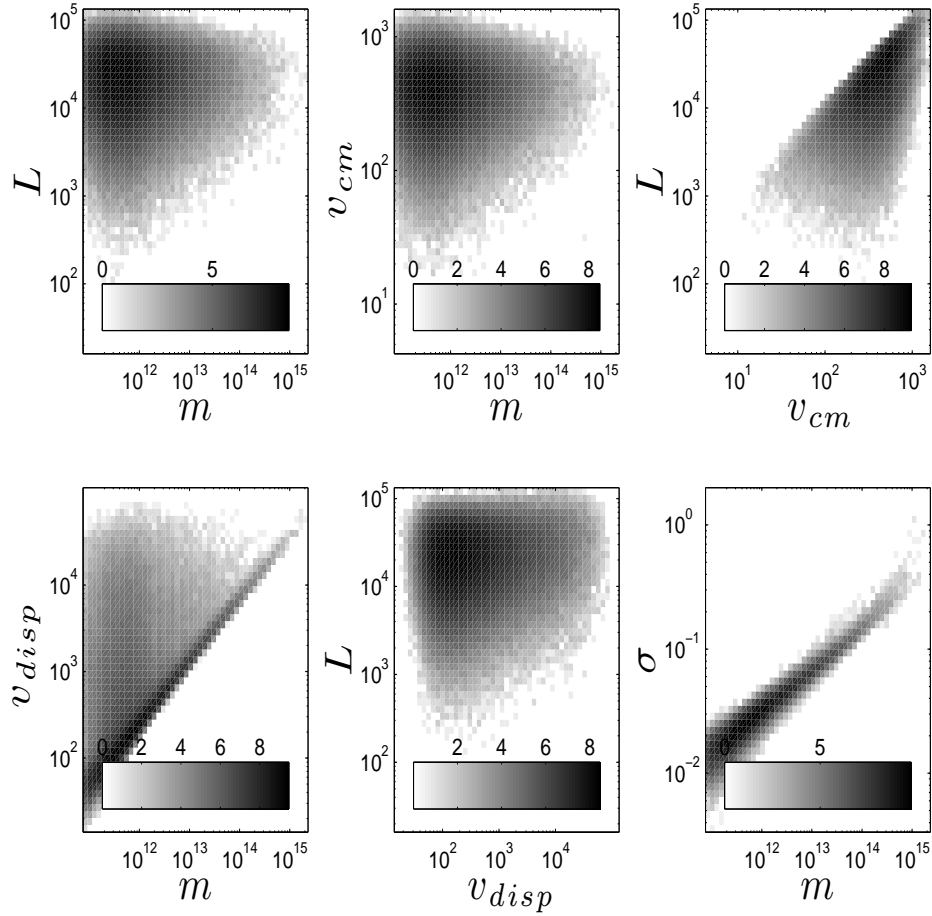


Figure 21. Halo properties at $z=0.961$. The mass is in M_{\odot} , the velocity is in km s^{-1} , the distances in $h^{-1}\text{Mpc}$, and the angular momentum in $h^{-1}\text{Mpc km s}^{-1}$.

Meiksin A., White M., 1999, MNRAS, 308, 1179
 Merz H., Pen U.-L., Trac H., 2005, New Astronomy, 10, 393
 Neyrinck M. C., Szapudi I., Rimes C. D., 2006, MNRAS, 370, L66
 Ngan W.-H. W., Harnois-Déraps J., Pen U.-L., MacDonald P., MacDonald I., 2011, ArXiv e-prints (astro-ph/1106.5548)
 Percival W. J., Cole S., Eisenstein D. J., Nichol R. C., Peacock J. A., Pope A. C., Szalay A. S., 2007, MNRAS, 381, 1053
 Percival W. J., et al., 2001, MNRAS, 327, 1297
 Planck Collaboration Ade P. A. R., Aghanim N., Arnaud M., Ashdown M., Aumont J., Baccigalupi C., Baker M., Balbi A., Banday A. J., et al. 2011, ArXiv e-prints
 Premadi P., Martel H., Matzner R., 1998, ApJ, 493, 10
 Press W. H., Schechter P., 1974, ApJ, 187, 425
 Rimes C. D., Hamilton A. J. S., 2005, MNRAS, 360, L82
 Sato M., Hamana T., Takahashi R., Takada M., Yoshida N., Matsubara T., Sugiyama N., 2009, ApJ, 701, 945
 Sato M., Takada M., Hamana T., Matsubara T., 2011, ApJ, 734, 76
 Schneider M. D., Bridle S., 2010, MNRAS, 402, 2127
 Schneider P., 1996, MNRAS, 283, 837
 Schneider P., van Waerbeke L., Jain B., Kruse G., 1998,

MNRAS, 296, 873
 Scoccimarro R., Sheth R. K., 2002, MNRAS, 329, 629
 Scranton R., Ménard B., Richards G. T., Nichol R. C., Myers A. D., Jain B., Gray A., Bartelmann M., Brunner R. J., Connolly A. J., Gunn J. E., Sheth R. K., Bahcall N. A., Brinkman J., Loveday J., Schneider D. P., Thakur A., York D. G., 2005, ApJ, 633, 589
 Seljak U., Zaldarriaga M., 1996, ApJ, 469, 437
 Semboloni E., Heymans C., van Waerbeke L., Schneider P., 2008, MNRAS, 388, 991
 Semboloni E., Hoekstra H., Schaye J., van Daalen M. P., McCarthy I. G., 2011, MNRAS, 417, 2020
 Semboloni E., Mellier Y., van Waerbeke L., Hoekstra H., Tereno I., Benabed K., Gwyn S. D. J., Fu L., Hudson M. J., Maoli R., Parker L. C., 2006, A&A, 452, 51
 Semboloni E., Schrabback T., van Waerbeke L., Vafaei S., Hartlap J., Hilbert S., 2011, MNRAS, 410, 143
 Shandarin S. F., Zeldovich Y. B., 1989, Reviews of Modern Physics, 61, 185
 Sheth R. K., Tormen G., 2002, MNRAS, 329, 61
 Smith R. E., Peacock J. A., Jenkins A., White S. D. M., Frenk C. S., Pearce F. R., Thomas P. A., Efsthathiou G., Couchman H. M. P., 2003, MNRAS, 341, 1311
 Takada M., Jain B., 2009, MNRAS, 395, 2065
 Takahashi R., et al., 2009, ApJ, 700, 479

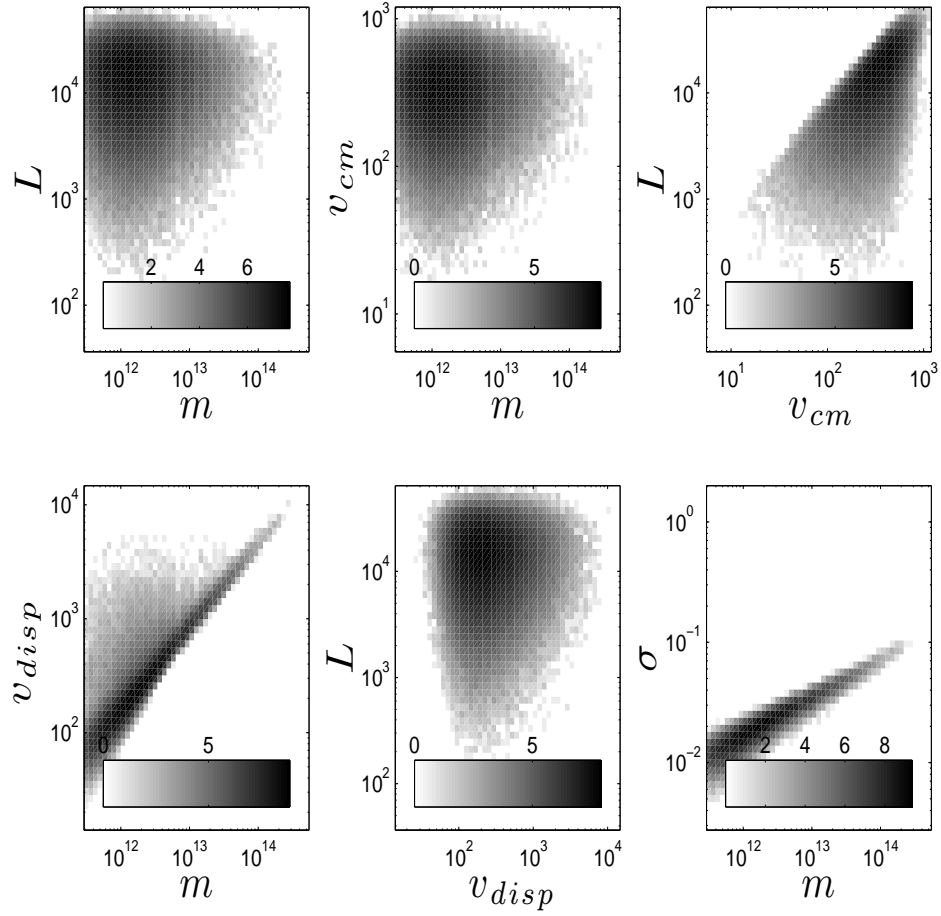


Figure 22. Halo properties at $z=3.004$. The mass is in M_{\odot} , the velocity is in km s^{-1} , the distances in $h^{-1}\text{Mpc}$, and the angular momentum in $h^{-1}\text{Mpc km s}^{-1}$.

Tegmark M., et al., 2006, Phys. Rev. D, 74, 123507
Vafaei S., Lu T., van Waerbeke L., Semboloni E., Heymans
C., Pen U.-L., 2010, Astroparticle Physics, 32, 340
Vale C., White M., 2003, ApJ, 592, 699
White M., Hu W., 2000, ApJ, 537, 1
York D. G., et al., 2000, AJ, 120, 1579
Zel'Dovich Y. B., 1970, A&A, 5, 84

This paper has been typeset from a \LaTeX file prepared by the author.